Stratospheric Modulation of Tropical Upper-Tropospheric Warming-Induced Circulation Changes in an Idealized General Circulation Model

Roland Walz,[a] Hella Garny,[a,b] and Thomas Birner[b,a]

[a] *Institut für Physik der Atmosphäre, Deutsches Zentrum für Luft- und Raumfahrt, Oberpfaffenhofen, Germany*
[b] *Meteorological Institute Munich, Ludwig Maximilians University of Munich, Munich, Germany*

ABSTRACT: The stratospheric polar vortex is dynamically coupled to the tropospheric circulation. Therefore, a better mechanistic understanding of this coupled system is important to interpret past and future circulation changes correctly. Previously, idealized simulations with a dry dynamical-core general circulation model and imposed tropical upper-tropospheric warming (TUTW) have shown that a critical warming level exists at which the polar vortex transitions from a weak and variable to a strong and stable regime. Here, we investigate the dynamical mechanism responsible for this regime transition and its influence on the troposphere by performing similar idealized experiments with (REF) and without a polar vortex (NPV). According to the critical-layer control mechanism, the strengthened upper flank of the subtropical jet in response to TUTW leads to an accelerated wave-driven residual circulation in both experiments. For the REF experiment, the stronger residual circulation is associated with changes in the lower-stratospheric thermal structure that are consistent with an equatorward shift of the polar vortex. At a certain threshold of TUTW in the REF experiment, the tropospheric jet and the stratospheric polar vortex form a confined waveguide for planetary-scale waves that presumably favors downward wave coupling events. Consistently, the polar vortex strengthens in combination with an enhanced poleward shift of the tropospheric jet compared to the NPV experiment. Overall, these idealized experiments suggest that a polar vortex strengthening can be caused by greenhouse gas–induced warmings via modifications of the waveguide. This mechanism might also be relevant to understand the polar vortex changes in more complex models.

KEYWORDS: Stratosphere-troposphere coupling; Climate change; Idealized models

1. Introduction

A robust feature of greenhouse gas–induced changes to the atmospheric temperature structure is enhanced tropical upper-tropospheric warming (TUTW; Vallis et al. 2015). The associated meridional temperature gradient together with that due to greenhouse gas–induced stratospheric cooling leads to accelerated upper flanks of the subtropical jets. As a consequence, critical layers for Rossby wave propagation in the lower stratosphere rise, inducing a strengthened shallow branch of the residual circulation (Shepherd and McLandress 2011)—a robust feature of climate change in model experiments of various complexity (Wang et al. 2012; Manzini et al. 2014; Hardiman et al. 2014; Abalos et al. 2021). In addition to strengthened upper flanks of the subtropical jets, the midlatitude eddy-driven tropospheric jets tend to shift poleward in both hemispheres in response to increased greenhouse gas concentrations (Barnes and Polvani 2013), for which various dynamical mechanisms have been proposed so far (Shaw 2019).

The stratospheric zonal-mean zonal wind response to increased greenhouse gas concentrations is much less clear. About 70% of the models forced with the representative concentration pathway 8.5 scenario contributing to the Coupled Model Intercomparison Project phase 5 (CMIP5) protocol (Taylor et al. 2012) predict a weakening of the Northern Hemisphere (NH) stratospheric polar vortex by the end of the twenty-first century, but there is substantial uncertainty even in the sign of this change (Manzini et al. 2014; Wu et al. 2019; Kretschmer et al. 2020). The uncertainty of future polar vortex states also remains in the more recent CMIP6 multi-model ensemble forced by an abrupt quadrupling of carbon dioxide concentrations (Ayarzagüena et al. 2020) which is connected to the large spread in the strengthening of the deep branch of the residual circulation (Abalos et al. 2021).

Additional complexity to the transient atmospheric climate change is added by the nonlinear response of the stratospheric circulation for two consecutive periods of identical global warming. In a large ensemble of a fully coupled general circulation model forced by a 1% increase in the carbon dioxide concentration per year, a weakening of the NH stratospheric polar vortex during the first period of 2 K global warming, but a strengthening during the second period is found (Manzini et al. 2018). A possible reason for the nonlinear polar vortex response is the decrease of Arctic amplification when Arctic sea ice vanishes in the second period of 2 K global warming (Kim et al. 2014; Kretschmer et al. 2020; Kim and Kim 2020). The NH polar vortex weakening is, however, also observed when Arctic amplification is suppressed by prescribed sea surface temperatures (Karpechko and Manzini 2017), challenging this mechanism. Due to the significant downward stratospheric influence on the tropospheric circulation during extended winter seasons, e.g., by the downward migration of extreme zonal-mean anomalies (Baldwin and Dunkerton 2001),

---

Corresponding author: Roland Walz, Roland.Walz@dlr.de

or by the reflection of upward-propagating planetary-scale Rossby waves (Perlwitz and Graf 2001), reliable projections of stratospheric climate change are vital. Otherwise, the full spectrum of possible stratospheric climate projections blurs the tropospheric evolution as shown by Simpson et al. (2018).

One strategy to gain better mechanistic understanding and to help clarify the varied atmospheric response to increased greenhouse gas concentrations is to reduce complexity (Held 2005; Maher et al. 2019), e.g., by employing dry general circulation models driven by a relaxation to prescribed equilibrium temperatures mimicking radiative and convective effects (Held and Suarez 1994; Garny et al. 2020). Previously, idealized general circulation models have been used to study impacts of the polar vortex strength on the tropospheric circulation (Polvani and Kushner 2002; Gerber and Polvani 2009) and its interaction with the residual circulation (Gerber 2012) as well as sudden stratospheric warmings (Lindgren et al. 2018; Martineau et al. 2018) and climate change like thermal forcings as Arctic amplification or TUTW (Butler et al. 2010). In a similar manner, Wang et al. (2012) found nonlinear circulation changes of the coupled troposphere–stratosphere system in response to TUTW. For weak warming of the tropical upper troposphere, the strength of the polar vortex stays constant, but the residual circulation strengthens. At a critical threshold of TUTW, however, the polar vortex strengthens accompanied by a weakening of the residual circulation. Simultaneously, eddy-driven jets are shifted poleward by 10°, and previously upward-propagating wave activity is refracted equatorward within the troposphere.

This regime transition observed in idealized model simulations might be relevant for understanding the nonlinear climate change response in more complex models described above. To this end, we aim for a better understanding of the dynamical mechanism that is responsible for the regime transition found by Wang et al. (2012). We reproduce the experiment of Wang et al. (2012) and extend their simulations by changing the stratospheric basic state in two additional TUTW experiments. One additional experiment is designed to test the sensitivity of the circulation response to the stratospheric basic state, while the other experiment is designed to have a passive stratosphere which allows quantification of the influence of the polar vortex on the tropospheric circulation.

This paper is organized as follows. Section 2 presents guiding hypotheses regarding the dynamical mechanism to structure our analysis. Section 3 describes the idealized model and the TUTW experiments used in this study. Section 4 reports the circulation response to TUTW for the three experiments with different stratospheric basic states, and defines observed dynamical regimes. Sections 5–8 test the proposed hypotheses and contribute details to the dynamical mechanism responsible for the regime transition. In section 9, the robustness of previous results is evaluated by employing different resolutions, a different tropospheric stratification, and a different tropical heating shape. Section 10 discusses implications within the dynamical mechanism that require further investigations, and section 11 summarizes our conclusions.

2. Guiding hypotheses

To reveal the dynamical mechanism responsible for the polar vortex regime transition in idealized model simulations in response to sufficiently strong TUTW as reported in Wang et al. (2012), the hypotheses stated below will be tested. Along the way, details of the dynamical mechanism are added to establish the schematic displayed in Fig. 1. Assuming the tropospheric response to TUTW consists of a poleward shift of the tropospheric jets with accelerated upper flanks (highlighted in red in Fig. 1), we hypothesize the following:

1) TUTW leads to a strengthened shallow branch of the residual circulation consistent with the critical-layer control mechanism in the experiments with and without a polar vortex (gray boxes in Fig. 1; Shepherd and McLandress 2011).

2) In presence of a polar vortex, the strengthened shallow branch of the residual circulation influences the thermal structure of the lower stratosphere around 100 hPa, which is consistent with an equatorward shift of the lower-stratospheric polar vortex (green box in Fig. 1; Butchart et al. 2010; Scaife et al. 2012).

3) Given the importance of the lower stratosphere for troposphere–stratosphere coupling (Birner and Albers 2017; Martineau et al. 2018), the changing thermal structure of the lower stratosphere leads to a reorganization of Eliassen–Palm (EP) fluxes with less wave activity propagating into the stratosphere and more wave activity being refracted equatorward in the troposphere at a critical TUTW level associated with a sharp strengthening of the polar vortex as found by (Wang et al. 2012; blue box in Fig. 1).

4) Beyond the critical TUTW level, the increased strength of the stratospheric polar vortex leads to an enhanced poleward shift of the tropospheric jet (Polvani and Kushner 2002; Kidston et al. 2015).

3. Model and methodology

a. Model

We use the dry dynamical-core model ECHAM/MESSy Idealized model (EMIL; Garny et al. 2020) to analyze circulation changes in response to TUTW for three different stratospheric basic states. The model is set up following previous idealized general circulation models (Held and Suarez 1994; Polvani and Kushner 2002); i.e., EMIL uses Newtonian damping to relax temperatures toward a selected equilibrium temperature profile and Rayleigh friction to account for wind damping close to the surface and at the model top. The wind damping of the surface layer is identical to Held and Suarez (1994), but the wind damping at the model top deviates from Polvani and Kushner (2002) and follows a function that resembles drag by gravity waves more closely [Eq. (A9) in Garny et al. 2020]. The inverse relaxation time scale is also identical to Held and Suarez (1994). All experiments in this study are generated by variations of the equilibrium temperature profile and additional heating in the tropical upper troposphere (Butler et al. 2010; Wang et al. 2012). To induce a more realistic stratospheric circulation strength, planetary-
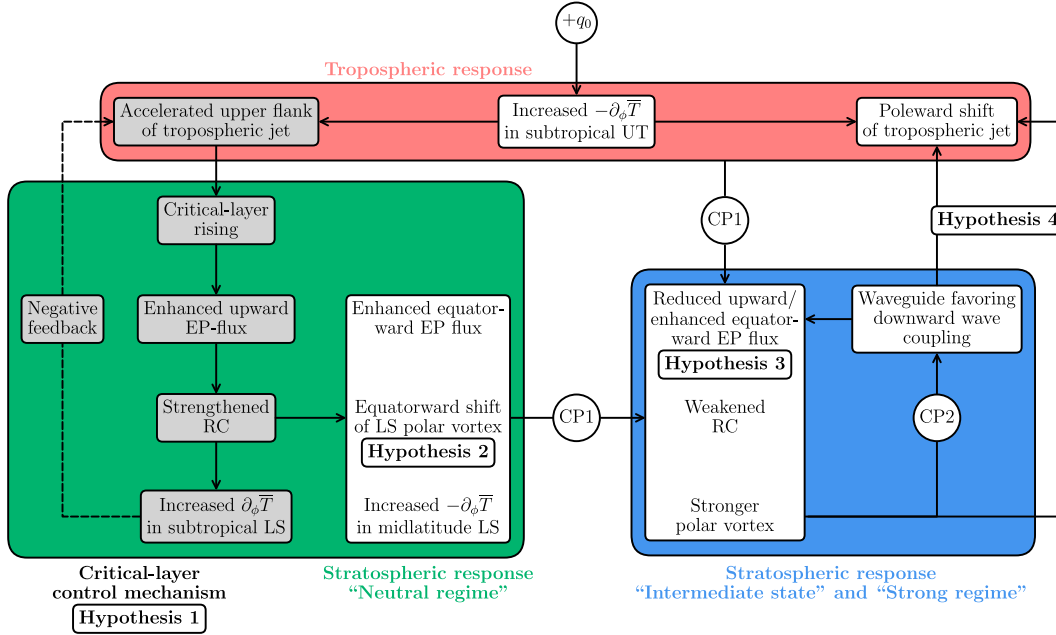
FIG. 1. Schematic of the dynamical mechanism responsible for the regime transition from a weak and variable to a strong and stable polar vortex and the corresponding impact on the troposphere in the idealized model experiments with a polar vortex (REF and CLS) forced by tropical upper-tropospheric heating of amplitude q_0. Stronger temperature gradients ($-\partial_\phi \overline{T}$) in the subtropical upper troposphere (UT) lead to both an accelerated upper flank and a poleward shift of the tropospheric jet (highlighted in red). Accelerated upper flanks are associated with increasing upward Eliassen–Palm (EP) flux, strengthening the residual circulation (RC) in the lower stratosphere (LS) via the critical-layer control mechanism [gray boxes on the left-hand side (hypothesis 1); Shepherd and McLandress 2011]. The strengthened shallow branch of the residual circulation affects the thermal structure of the lower stratosphere consistent with an equatorward shift of the polar vortex (hypothesis 2). For moderate heating amplitudes, the stratospheric response described above represents the neutral regime with a weak and variable polar vortex (highlighted in green). Beyond a first critical point (CP1; $q_0 \gtrsim 0.3$ K day^{-1} in the REF, $q_0 \gtrsim 0.05$ K day^{-1} in the CLS experiment, respectively), different dynamical regimes can be entered by further increases of q_0 (highlighted in blue). The changes in the upper troposphere and lower stratosphere eventually lead to a reorganization of EP fluxes, accompanied by a first weakening of the residual circulation and a strengthening of the polar vortex (hypothesis 3, Wang et al. 2012). In this intermediate state, moderately enhanced poleward shifts of the tropospheric jet can already be observed (hypothesis 4) compared to the experiment without a polar vortex (NPV). Beyond the second critical point (CP2; $q_0 \gtrsim 0.4$ K day^{-1} in the REF, $q_0 \gtrsim 0.1$ K day^{-1} in the CLS experiment, respectively), a confined geometry of the waveguide for planetary-scale waves is developed, which presumably favors downward wave coupling events (Perlwitz and Harnik 2003; Shaw et al. 2010), and the polar vortex enters the strong regime. Corresponding to a strong and stable polar vortex, enhanced poleward shifts of the tropospheric jet persist (hypothesis 4).

scale waves are generated by an idealized wavenumber-2 topography with an amplitude of 3 km between 25° and 65°N as in Gerber and Polvani (2009).

b. Equilibrium temperature profile

The equilibrium temperature profile is very similar to the one introduced by Polvani and Kushner (2002) and represents perpetual January conditions. In their profile, the transition in the equilibrium temperature from tropospheric to stratospheric schemes occurs at a constant pressure of $p_T \equiv 100$ hPa in both hemispheres. In EMIL, this transition pressure is a function of latitude ϕ and reads

$$p_T(\phi) = (p_{Tw} - p_{Ts})W(\phi) + p_{Ts}, \qquad (1)$$

with transition pressures p_{Ts} and p_{Tw} in the summer and winter hemispheres, respectively, where $p_{Ts} = 100$ hPa is held

fixed in this study. The weighting function $W(\phi)$ is identical to Polvani and Kushner (2002) which was introduced to perform a smooth transition from increasing temperature with height in the lower stratosphere of the summer hemisphere to decreasing temperature with height throughout the entire stratosphere of the winter hemisphere (Fig. 2b). The strength of this temperature decrease with height in the winter-hemispheric stratosphere is determined by the polar vortex lapse rate γ. Employing the latitudinally dependent transition pressure $p_T(\phi)$ given in Eq. (1) allows one to vary the onset of the polar vortex lapse rate in the winter hemisphere without interfering with the tropospheric temperature scheme.

The two stratospheric basic states with a polar vortex are defined by p_{Tw} and γ. The reference experiment (REF) employs $p_{Tw} = 100$ hPa as well as $\gamma = 4$ K km^{-1} (Fig. 2b) and exhibits realistic troposphere–stratosphere coupling (Gerber

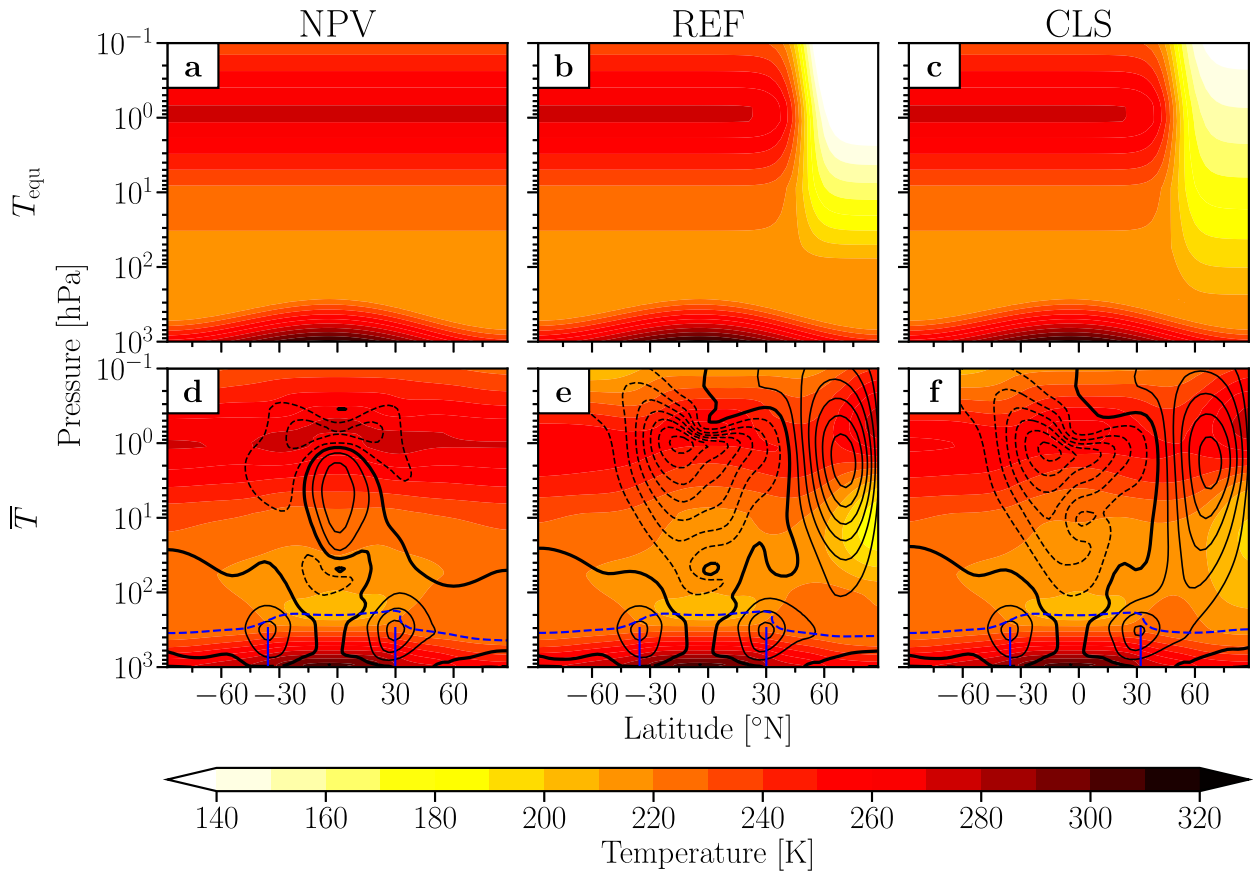FIG. 2. (a)–(c) Zonally symmetric equilibrium temperatures T_{equ} and (d)–(f) zonally averaged simulated temperature climatologies $\overline{T}$ as functions of latitude and pressure (color shading with a contour interval of 10 K) for the (a),(d) NPV, (b),(e) REF, and (c),(f) CLS control runs ($q_0 = 0$). In (d)–(f), zonally averaged zonal wind climatologies (black contour lines with a contour interval of 10 m s^{-1}, negative contours dashed, thick zero-contour line), lapse-rate tropopauses (blue dashed lines; WMO 1957), and latitudes of tropospheric wind maxima (blue solid vertical lines) are added.

and Polvani 2009). Since temperatures in the lower stratosphere of the polar winter hemisphere are known to be too warm in simulations with REF conditions (compared to observations; Sheshadri et al. 2015; Garny et al. 2020), a sensitivity experiment with a polar vortex is performed with a colder lower stratosphere (CLS) by employing $p_{\mathrm{Tw}} = 400$ hPa and $\gamma = 2$ K km^{-1} (Fig. 2c). These parameters defining the stratospheric basic state of the CLS experiment were found in a parameter-sweep experiment intended to create a more realistic temperature profile in the polar lower stratosphere (Garny et al. 2020).[1] Here, we choose $p_{\mathrm{Tw}} = 400$ hPa and $\gamma = 2$ K km^{-1} for the CLS experiment to reach a mean polar vortex strength that is similar to the REF experiment as shown in Figs. 3b and A1a for both control runs (without additional tropical

upper-tropospheric heating). The probability density function of the polar vortex strength in the CLS control run, however, deviates from observations and exhibits a double-peak structure (Fig. A1a) which in turn is consistent with a higher and more realistic frequency of sudden stratospheric warmings (Fig. A1b).[2] These differences between the REF and the CLS control runs confirm that troposphere–stratosphere coupling is very sensitive to changes in the polar lower stratosphere (Martineau et al. 2018). Nevertheless, the overall purpose of the CLS experiment is not to create a setup that is more realistic in every aspect, but to provide a sensitivity experiment to test the dynamical mechanism proposed in this study. In contrast to the REF and CLS experiments, the third experiment does not include a polar vortex (NPV) which is achieved by setting $W(\phi) \equiv 0$ in the stratospheric equilibrium temperature and which also implies $p_T \equiv 100$ hPa (Fig. 2a; also refer to paragraph 22 in the appendix of Polvani and Kushner 2002).

---

[1] The parameter p_{Tw} can influence the tropopause height in the polar lower stratosphere. Note, however, that p_{Tw} does not fix the tropopause in the polar lower stratosphere directly, which is instead dynamically formed. In fact, the tropopause in the CLS control run is slightly higher than in the REF control run in the polar lower stratosphere (see Figs. 2e,f).

[2] Computational details for the sudden stratospheric warming frequency are given in appendix A.
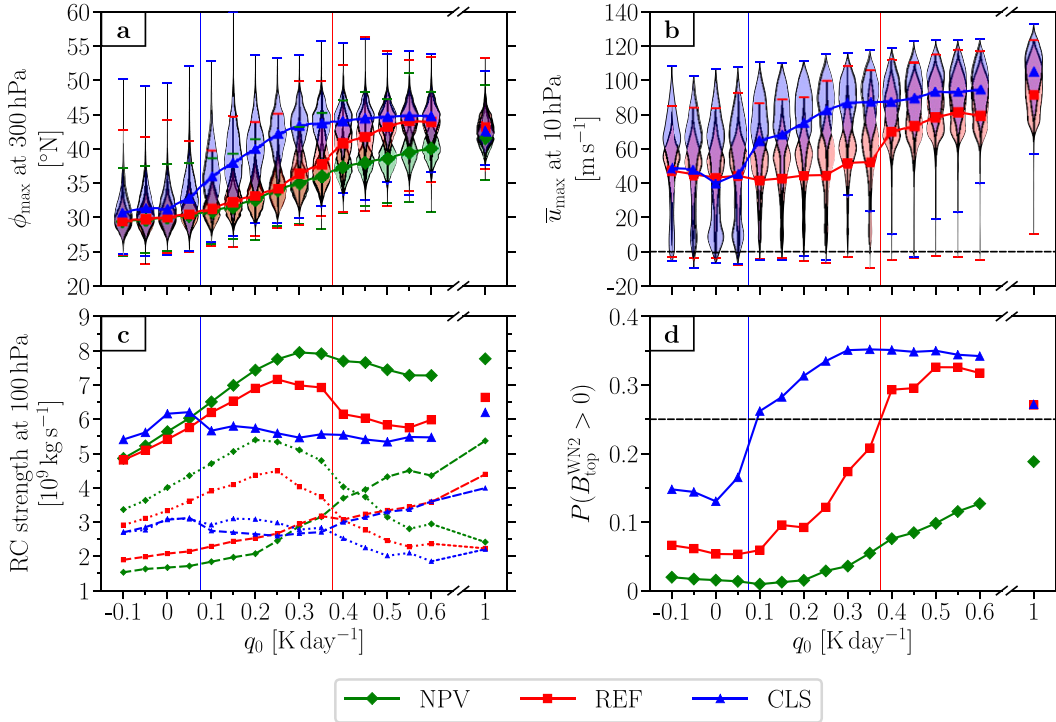
FIG. 3. (a) Latitude ϕ_{max} of the NH maximum zonal-mean zonal wind at 300 hPa, (b) strength $\overline{u}_{max}$ of the NH maximum zonal-mean zonal wind at 10 hPa, (c) strength of the residual circulation (RC) at 100 hPa with contributions from planetary- (dashed, zonal wavenumbers 1–3) and synoptic-scale (dotted, zonal wavenumbers larger than 3) EP flux divergence, and (d) the probability P that the wavenumber-2 vertical EP flux B_{top}^{WN2} at 100 hPa integrated from 40° to 60°N is downward as functions of the tropical upper-tropospheric heating amplitude q_0 for the NPV, REF, and CLS experiments. Colored markers display values of ϕ_{max} and $\overline{u}_{max}$ that are computed from climatological-mean zonal-mean zonal winds. Additionally, the shapes of the probability distribution functions (colored shading) and extreme values (colored horizontal lines) are provided for which ϕ_{max} and $\overline{u}_{max}$ are computed for every time step first. Note that all probability distributions are scaled in such a way that they have equal widths at their respective maxima. Red and blue vertical lines indicate the transitions to the strong polar vortex regime in the REF and CLS experiments, respectively.

Tropospheric equilibrium temperatures are identical for the NPV, REF, and CLS experiments. For the primary set of simulations in sections 4–8, the parameter δ_z which determines the vertical temperature gradient in the troposphere is set to $\delta_z = 4.3$ K due to an implementation error (Garny et al. 2020).[3] To guarantee robust results, some simulations are repeated with the original value of $\delta_z = 10$ K in section 9 (Held and Suarez 1994). As temperature differences due to different values of δ_z are most pronounced in the tropical upper troposphere (Fig. 2b in Garny et al. 2020), circulation changes in TUTW experiments with different δ_z are very similar and only appear at different heating amplitudes which will be shown in section 9. Together with tropical upper-tropospheric heating which will be introduced in the following, the REF experiment in combination with $\delta_z = 10$ K

represents the same experiment as already conducted by Wang et al. (2012).

c. Tropical upper-tropospheric heating

In addition to relaxation toward respective equilibrium temperatures of the NPV, REF, and CLS experiments maintaining the corresponding basic states, temperature tendencies are extended by TUTW. To this end, we employ in sections 4–8 the thermal forcing introduced by Butler et al. (2010) and also used by Wang et al. (2012) which is given by

$$Q(\phi, p) = q_0 \exp\left[-\frac{1}{2}\left(\frac{\phi}{0.4}\frac{\pi}{180°}\right)^2 - \frac{1}{2}\left(\frac{p/p_{surf} - z_0}{0.11}\right)^2 \right], \quad (2)$$

where q_0 is the heating amplitude, ϕ is latitude in degrees north, p is pressure, p_{surf} is surface pressure, and $z_0 = 0.3$ is the fraction of the surface pressure at which the thermal forcing is centered. Butler et al. (2010) used a fixed heating amplitude of $q_0 = 0.5$ K day^{-1}, whereas Wang et al. (2012) varied q_0 from -0.1 to 0.5 K day^{-1}. Similarly, we apply thermal

---

[3] Instead of the natural logarithm, a logarithm with base 10 was implemented in the tropospheric equilibrium temperature, scaling the magnitude of the original value of $\delta_z = 10$ K by a factor of $1/\ln(10) \approx 0.43$ (Garny et al. 2020).

TABLE 1. List of simulations used in this study that are performed with the dry dynamical-core model EMIL (Garny et al. 2020). Circulation changes induced by different tropical upper-tropospheric heating amplitudes q_0 are evaluated for three different stratospheric conditions: one reference setup with a polar vortex and realistic troposphere–stratosphere coupling (REF), one sensitivity setup with a polar vortex with a colder polar lower stratosphere (CLS), and one setup without a polar vortex (NPV).

Stratospheric condition	Name	Resolution	Heating amplitudes q_0 (K day^{-1})	Heating shape	Stratification δ_z (K)
NPV	NPV	T42L90	−0.1, −0.05, 0, 0.05, 0.1, 0.15, 0.2, 0.25, 0.3, 0.35, 0.4, 0.45, 0.5, 0.55, 0.6, 1	Standard, Eq. (2)	4.3
	NPV-L47	T42L47	−0.1, 0, 0.1, 0.2, 0.3, 0.4, 0.5, 0.6, 1	Standard, Eq. (2)	4.3
	NPV-T85	T85L47	0, 0.15, 0.2, 0.25, 0.3, 0.35, 0.4, 0.45, 0.5, 0.6, 1	Standard, Eq. (2)	4.3
	NPV-d10	T85L47	0, 0.05, 0.1, 0.15, 0.2, 0.25, 0.3, 0.35, 0.4, 0.5, 1	Standard, Eq. (2)	10
REF	REF	T42L90	−0.1, −0.05, 0, 0.05, 0.1, 0.15, 0.2, 0.25, 0.3, 0.35, 0.4, 0.45, 0.5, 0.55, 0.6, 1	Standard, Eq. (2)	4.3
	REF-L47	T42L47	−0.1, 0, 0.1, 0.2, 0.3, 0.4, 0.5, 0.6, 1	Standard, Eq. (2)	4.3
	REF-T85	T85L47	0, 0.15, 0.2, 0.25, 0.3, 0.35, 0.4, 0.45, 0.5, 0.6, 1	Standard, Eq. (2)	4.3
	REF-d10	T85L47	0, 0.05, 0.1, 0.15, 0.2, 0.25, 0.3, 0.35, 0.4, 0.5, 1	Standard, Eq. (2)	10
	REF-mod	T85L47	0.2, 0.4, 0.5, 0.6, 0.7, 0.8, 1, 1.2	Modified, Eq. (3)	4.3
CLS	CLS	T42L90	−0.1, −0.05, 0, 0.05, 0.1, 0.15, 0.2, 0.25, 0.3, 0.35, 0.4, 0.45, 0.5, 0.55, 0.6, 1	Standard, Eq. (2)	4.3
	CLS-T85	T85L47	−0.1, −0.05, 0, 0.05, 0.1, 0.15, 0.2, 0.3, 0.5	Standard, Eq. (2)	4.3

forcings in the form of Eq. (2) with heating amplitudes ranging from −0.1 to 1 K day^{-1}.

To investigate the influence of a more rapid decrease of the heating strength away from its vertical center z_0, in particular to exclude the tropical lower stratosphere from heating, we also test a modified thermal forcing in section 9 which is of the form

$$\tilde{Q}(\phi, p) = q_0 \exp\left\{ -\frac{1}{2}\left(\frac{\phi}{0.4}\frac{\pi}{180°}\right)^2 - \frac{1}{2}\left[\frac{\ln(p/p_{\mathrm{surf}}) - \ln(z_0)}{0.18}\right]^2 \right\}. \tag{3}$$

The results of sections 4–8 are based on simulations with a resolution of T42L90, whereas section 9 additionally employs simulations at resolutions T42L47 and T85L47. All simulations are integrated for 9950 days after 1000 days of spinup at time steps between 360 and 540 s. A list of all experiments with corresponding settings for important parameters is given in Table 1.

4. Circulation response to TUTW and definition of polar vortex regimes

The zonal-mean zonal wind control-run climatologies of the NPV, REF, and CLS experiments without additional tropical upper-tropospheric heating ($q_0 = 0$) are shown in Figs. 2d–f. In the winter hemisphere, the tropospheric jet maxima at 300 hPa are located at 30°N in the NPV and REF experiments as well as at 32°N in the CLS experiment, respectively (see also Fig. 3a). The polar vortex of the CLS experiment is weaker in the upper stratosphere, but stronger and equatorward shifted in the lower stratosphere compared to the REF experiment due to the colder polar lower

stratosphere of the CLS experiment. By construction, there is no stratospheric polar vortex in the NPV experiment, but an additional jet appears in the tropical upper stratosphere, which has no influence on the results of this study (section 9) and which disappears if only 47 vertical model levels are used instead of 90 (not shown).

In response to TUTW, the latitude $\phi_{\max}$ of the NH tropospheric jets increases in all three experiments (Fig. 3a). The major difference between the two experiments with a polar vortex and the one without is the pronounced poleward shift of the tropospheric jet occurring at the same heating amplitude as the sharp increase of the polar vortex strength $\overline{u}_{\max}$ at 10 hPa (Fig. 3b) which is accompanied by a decrease in the residual circulation strength at 100 hPa (Fig. 3c) and by an increase in the probability P of downward wavenumber-2 wave flux events in the midlatitude lower stratosphere (Fig. 3d).[4] Polar vortex strengthening and residual circulation weakening at a critical heating amplitude have already been found by Wang et al. (2012), who have also observed a reorganization of wave fluxes accompanying the regime transition with less wave activity propagating into the stratosphere and more wave activity being refracted equatorward in the troposphere. Here, we aim for the dynamical mechanism explaining this regime transition. To this end, we first define different regimes on the basis of Fig. 3.

In the REF experiment, climate states generated by $q_0 \leq 0.25$ K day^{-1} are defined as the neutral polar vortex regime since $\overline{u}_{\max}$ stays approximately constant and $\phi_{\max}$

---

[4] Computational details for $\phi_{\max}$, the residual circulation strength, and wave fluxes associated with a closed region are given in appendixes B, C, and D, respectively.

does not significantly deviate from the NPV experiment. In this regime, the residual circulation steadily strengthens with increasing q_0 and downward wavenumber-2 fluxes are rare. For $0.3 \leq q_0 \leq 0.35$ K day^{-1}, an intermediate state can be observed with a first increase in the polar vortex strength, a modest decrease in the residual circulation strength, more frequent downward wave flux events, and slightly enhanced poleward fluctuations of the tropospheric jet compared to the NPV experiment. The probability distribution functions of ϕ_{max}, however, still overlap to a large extent for the NPV and REF experiments. Climate states generated by $q_0 \gtrsim 0.4$ K day^{-1} are defined as the strong polar vortex regime by $\overline{u}_{max} > 60$ m s^{-1}, by $P > 0.25$, and by a sharp weakening of the residual circulation strength.[5] The narrower probability distribution functions of $\overline{u}_{max}$ at small wind speeds suggest that sudden stratospheric warmings or weak states of the polar vortex are extremely rare in the strong polar vortex regime, which is confirmed by Fig. A1b. Furthermore, an enhanced poleward shift of the tropospheric jet compared to the jet of the NPV experiment occurs.

In the CLS experiment, the circulation response to TUTW is similar to the REF experiment, but shifted to smaller q_0. The neutral polar vortex regime is defined by heating amplitudes of $q_0 \leq 0$ due to the constant offset of ϕ_{max} compared to the NPV experiment and the strengthening residual circulation. At $q_0 = 0.05$ K day^{-1}, an intermediate state is observed with slightly enhanced poleward fluctuations of the tropospheric jet compared to the NPV experiment and a first increase in the polar vortex strength. Analogous to the REF experiment, the strong polar vortex regime in the CLS experiment is defined by heating amplitudes of $q_0 \gtrsim 0.1$ K day^{-1} exhibiting $\overline{u}_{max} > 60$ m s^{-1}, $P > 0.25$, and a sharp weakening of the residual circulation strength compared to the intermediate state. The transition to the strong polar vortex regime is shifted to smaller heating amplitudes since the control-run climatology of the CLS experiment is already very close to the regime transition (Garny et al. 2020). The disappearance of probabilities of weak polar vortex states in the CLS experiment does, however, not happen as rapidly as in the REF experiment (see also Fig. A1b).

To simplify the evaluation of the hypotheses of section 2 in the following sections, we will confine ourselves to the NPV and REF experiments. The dynamical evolution in the CLS experiment will be used to test the proposed mechanism in section 9.

5. Hypothesis 1: Critical-layer control mechanism

In the control run of the NPV experiment, the absence of stratospheric westerlies inhibits wave propagation in the stratosphere, leading to a broad region of wave dissipation above the tropospheric jet in the lower stratosphere which extends over the entire hemisphere with maximum dissipation poleward of 20°N (Fig. 4a). Planetary-scale wave fluxes contribute strongest between 40° and 70°N (Fig. 4b), whereas synoptic-scale wave fluxes contribute strongest between 25° and 45°N, which is closer to the lower-stratospheric turnaround latitudes of the streamfunction (Fig. 4c).[6] Accordingly, synoptic-scale waves contribute more strongly to the strength of the lower-stratospheric residual circulation, at least for $q_0 \lesssim 0.4$ K day^{-1} (Fig. 3c). In response to TUTW, the upper flank of the tropospheric jet accelerates (e.g., Figs. 4a,d,g) causing the regions of wave dissipation of both planetary- (Figs. 4b,e,h) and synoptic-scale (Figs. 4c,f,i) waves to move upward. In terms of planetary-scale waves, which can be assumed to be stationary (Matsuno 1970), the rising zero-wind layer translates to stronger wave driving of the stratosphere consistent with the critical-layer control mechanism (Shepherd and McLandress 2011). Although the exact location of the critical layer for synoptic-scale waves is not known due to their nonzero phase speeds (Randel and Held 1991), we assume that the critical-layer control mechanism is also present for synoptic-scale waves.

Due to the dissipation of synoptic-scale waves close to lower-stratospheric turnaround latitudes in the control run ($q_0 = 0$), an upward shift of this region of dissipation is directly transferred to a strengthening of the residual circulation up to $q_0 = 0.2$ K day^{-1} (Fig. 3c). For larger heating amplitudes shifting the tropospheric jet sufficiently poleward, the critical-layer control mechanism for synoptic-scale waves loses efficiency consistent with less synoptic-scale wave flux reaching its critical layer and being instead refracted equatorward within the troposphere (Fig. 4i). Consequently, the contribution of synoptic-scale waves to the residual circulation strength in the lower stratosphere starts to decrease for $q_0 > 0.2$ K day^{-1} (Fig. 3c). In contrast to synoptic-scale waves, the region of strongest planetary-scale wave dissipation in the control run ($q_0 = 0$) is located poleward of the turnaround latitudes (Fig. 4b). Indeed, rising critical layers are consistent with a continuous increase of upward planetary-scale wave flux (Fig. 4e), but up to $q_0 = 0.2$ K day^{-1}, planetary-scale wave dissipation still happens mainly poleward of the turnaround latitudes associated only with a moderate increase in the driving of the residual circulation in the lower stratosphere (Fig. 3c). At $q_0 = 0.25$ K day^{-1}, the tropospheric jet has reached a sufficiently poleward position in combination with a sufficient vertical extent, such that planetary-scale wave flux is refracted more equatorward to dissipate closer to the turnaround latitudes (Fig. 4h). Thus, the contribution of planetary-scale waves to the lower-stratospheric residual circulation strength is enhanced for $q_0 \gtrsim 0.25$ K day^{-1} (Fig. 3c).

---

[5] The values of $\overline{u}_{max}$ and P used to define the strong polar vortex regime should not be expected to be transferable to complex models or the real atmosphere. They only serve for the purpose of clearly identifying the strong polar vortex regime in these idealized model simulations.

[6] In this study, waves of zonal wavenumbers 1–3 are considered planetary scale, and waves of zonal wavenumbers larger than 3 are considered synoptic scale, respectively.
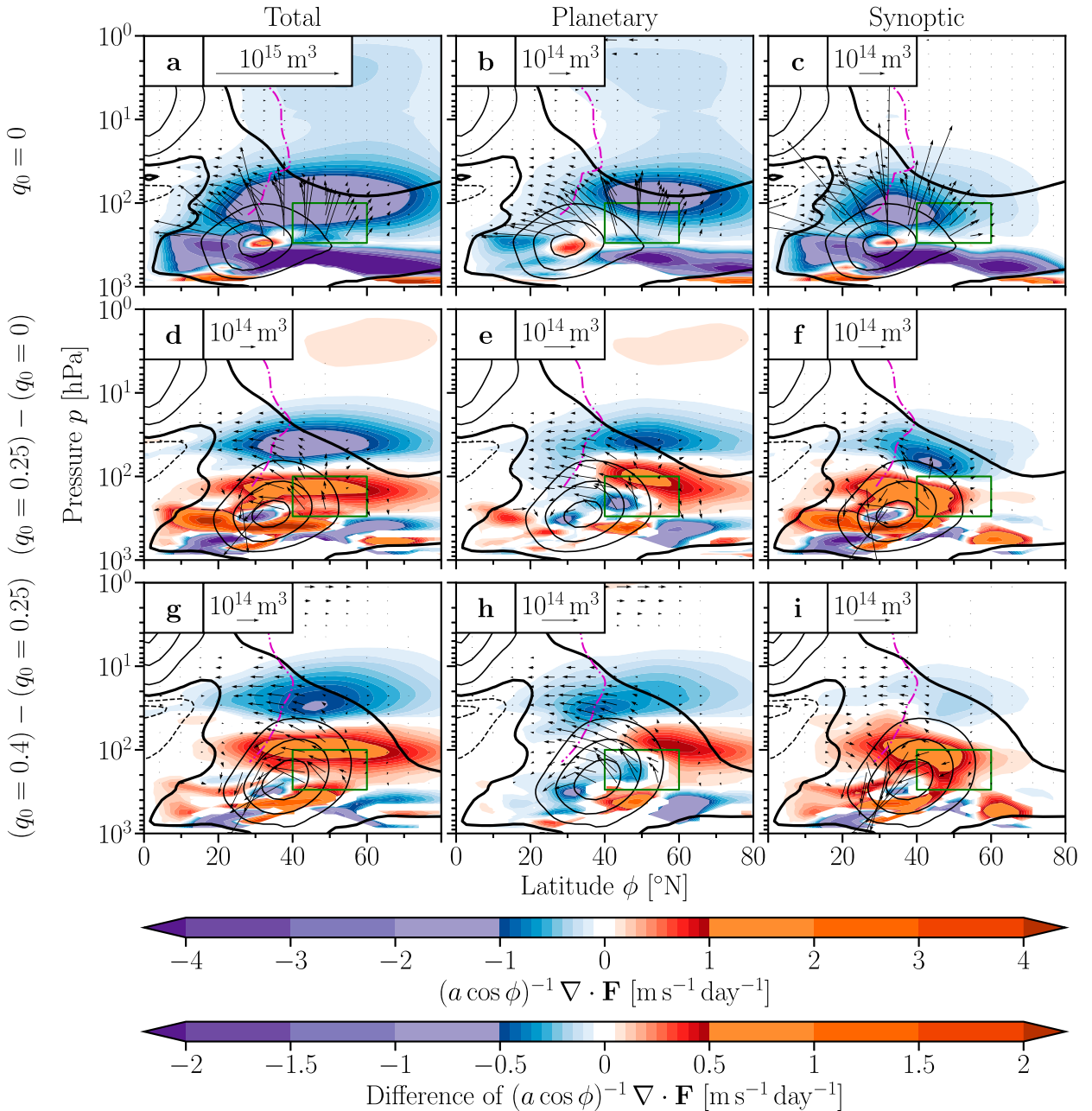
FIG. 4. (a) Control-run ($q_0 = 0$) tendencies of the zonal-mean zonal wind by the total EP flux divergence $(a\cos\phi)^{-1}\boldsymbol{\nabla}\cdot\mathbf{F}$ (color shading) and total EP flux arrows $\hat{\mathbf{F}} = (\hat{F}^{(\phi)}, \hat{F}^{(p)})$ (arrows) as functions of latitude and pressure, as well as (b) the contributions from planetary- (zonal wavenumbers 1–3) and (c) synoptic-scale (zonal wavenumbers larger than 3) EP fluxes for the NPV experiment. (d)–(i) Differences of the zonal-mean zonal wind tendencies and EP fluxes (d)–(f) between climate states at $q_0 = 0.25$ K day^{-1} and $q_0 = 0$ and (g)–(i) between $q_0 = 0.4$ and $q_0 = 0.25$ K day^{-1}. Only differences that are statistically significant at a 95% confidence level are shown. Zonal-mean zonal winds (black contour lines with a contour interval of 10 m s^{-1}, negative contours dashed, thick zero-contour line) and turnaround latitudes of the downward-control streamfunction Ψ_{dc}^* (magenta dash–dotted lines; Haynes et al. 1991) are added for (a)–(c) $q_0 = 0$, (d)–(f) $q_0 = 0.25$ K day^{-1}, and (g)–(i) $q_0 = 0.4$ K day^{-1}. EP flux arrows are defined as $(\hat{F}^{(\phi)}, \hat{F}^{(p)}) = 2\pi ag^{-1}\cos\phi[F^{(\phi)}, aF^{(p)}/(-80.4 \text{ kPa})]$ according to Edmon et al. (1980). The green boxes represent the region for which EP flux components are shown in Fig. D1.
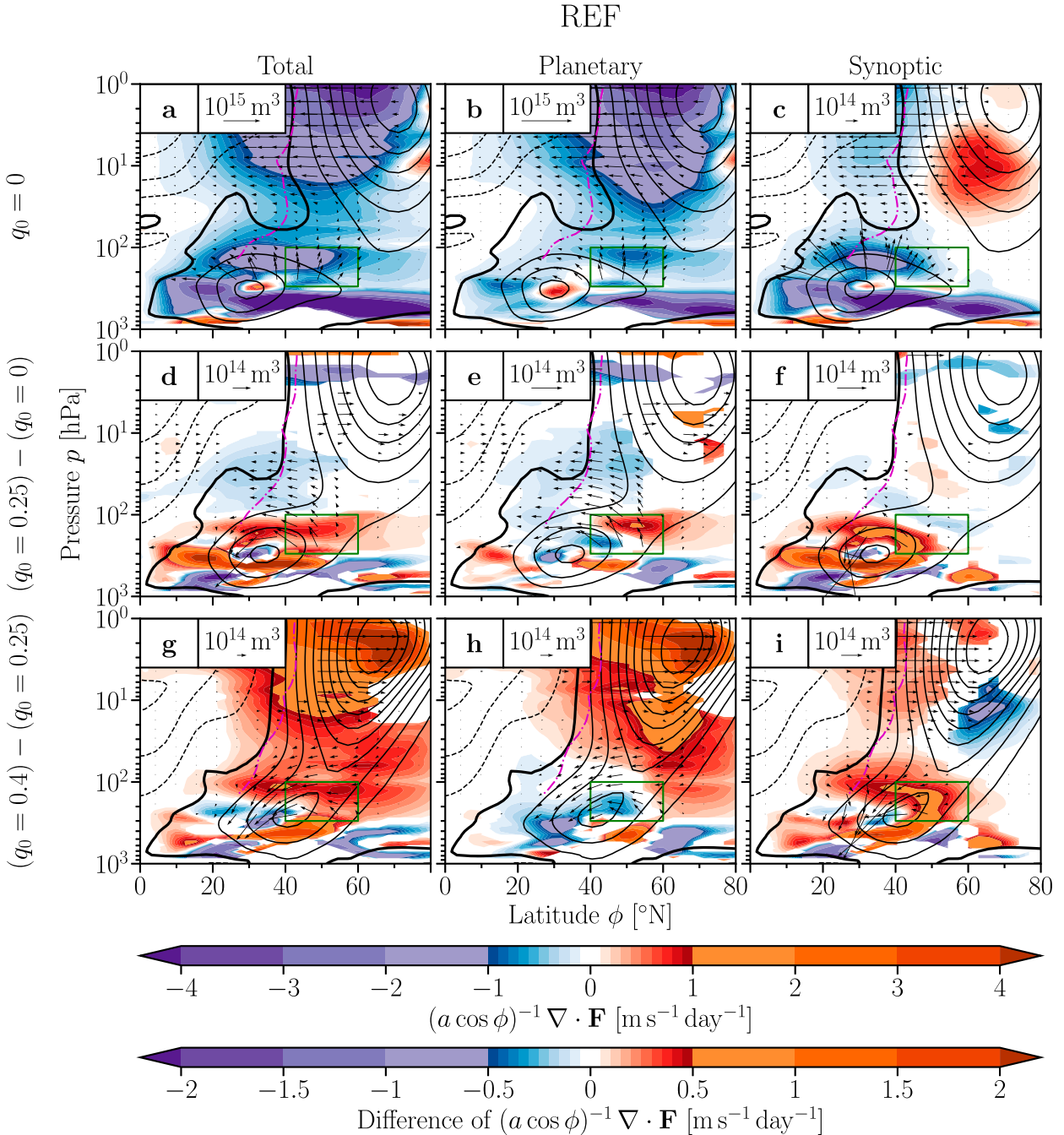
REF

FIG. 5. As in Fig. 4, but for the REF experiment.

In the control run of the REF experiment, the region of strongest wave dissipation above the tropospheric jet is confined to latitudes between 20° and 50°N (Fig. 5a) since planetary-scale wave activity is not subject to dissipate in the midlatitude lower stratosphere as in the control run of the NPV experiment (Fig. 4b), but is instead able to propagate further up into the stratosphere due to the waveguide provided by the polar vortex (Fig. 5b). Hence, planetary-scale waves are able to drive a stronger residual circulation in the upper

stratosphere compared to the NPV experiment. The residual circulation strength at 100 hPa is also predominantly driven by synoptic-scale waves, but increases slightly slower in the neutral polar vortex regime than in the NPV experiment up to $q_0 = 0.25$ K day^{-1} (Fig. 3c) associated with a smaller increase in synoptic-scale wave driving of the lower stratosphere close to the turnaround latitudes (Fig. 5f). The critical-layer control mechanism in the neutral polar vortex regime of the REF experiment is less efficient than in the

NPV experiment consistent with less synoptic-scale wave flux propagating poleward at 40°N (Fig. D1i) and upward at 100 hPa (Fig. D1f) to contribute to the driving of the residual circulation (Fig. 3c). Overall, the presence of a polar vortex reduces the TUTW-induced increase of total wave driving close to the lower-stratospheric turnaround latitudes in the neutral polar vortex regime.

The results above confirm hypothesis 1. In both experiments with and without a polar vortex (REF and NPV), the strengthened shallow branch of the residual circulation is consistent with the critical-layer control mechanism (gray boxes in Fig. 1). In the neutral polar vortex regime of the REF experiment and for weak heating amplitudes of the NPV experiment, the lower-stratospheric residual circulation is predominantly driven by synoptic-scale waves. Due to their nonvanishing phase speeds, however, a more involved analysis is necessary to confirm the critical-layer control mechanism for synoptic-scale waves (Randel and Held 1991; Shepherd and McLandress 2011).

6. Hypothesis 2: Equatorward shift of the lower-stratospheric polar vortex

Structural differences of the residual circulation between the experiments with and without a polar vortex are also reflected in different temperature signatures $\Delta \overline{T}_{q_0}$ that occur when the circulation is strengthened in response to TUTW. To translate these temperature signatures to a zonal wind that is in balance with $\Delta \overline{T}_{q_0}$, we consult the solution of the thermal wind equation in spherical coordinates:

$$\overline{u}_{\text{th}}(\Delta \overline{T}_{q_0}) = -\Omega a \cos(\phi)$$
$$+ \sqrt{[\overline{u}_{\text{bot}} + \Omega a \cos(\phi)]^2 + \frac{R}{\tan(\phi)} \int_{p_{\text{bot}}}^{p} \frac{\partial_\phi \Delta \overline{T}_{q_0}}{p'} dp'}, \tag{4}$$

where Ω and a are Earth's rotation rate and radius, respectively, R is the specific gas constant for dry air, and $\overline{u}_{\text{bot}} = 0$ is the zonal-mean zonal wind at the surface $p_{\text{bot}} = 1000$ hPa. Since we are interested in stratospheric temperature and corresponding zonal wind signatures, we employ

$$\Delta \overline{u}_{\text{th}} = \overline{u}_{\text{th}}(\Delta \overline{T}_{q_0}) - \overline{u}_{\text{th}}(\widetilde{\Delta \overline{T}_{q_0}}), \tag{5}$$

where modified temperature differences

$$\widetilde{\Delta \overline{T}_{q_0}} = \begin{cases} 0 & \text{for } p < 150 \text{ hPa} \\ \Delta \overline{T}_{q_0} & \text{for } p \geq 150 \text{ hPa} \end{cases} \tag{6}$$

are used in the subtrahend on the right-hand side of Eq. (5). As a result, $\Delta \overline{u}_{\text{th}}$ only contains the thermal-wind effect of stratospheric temperature differences above 150 hPa as shown in Fig. 6.

In the tropical tropopause region, both experiments exhibit approximately the same warming when forced with a heating amplitude of $q_0 = 0.25$ K day^{-1} (Figs. 6a,b). In the stratosphere,

$\Delta \overline{T}_{q_0}$ differs due to different structures of the residual circulation. In the NPV experiment, the entire extratropical lower stratosphere is subject to heating associated with the widespread region of downwelling poleward of the turnaround latitudes. In response to the TUTW-induced critical-layer rise, the region of strong wave dissipation is lifted consistent with stronger downwelling, hence heating, above 200 hPa, and weaker downwelling, hence cooling, below 200 hPa in the lower stratosphere as shown in Fig. 6a. Zonal-mean zonal winds are attenuated with increasing height in the region above the tropospheric jet due to the positive meridional temperature gradient in that region. The ongoing critical-layer rise due to TUTW in the NPV experiment leads to an expansion of the tropospheric jet in upward and poleward direction, but the structure of the residual circulation always exerts negative feedback on the upward expansion by a negative thermal-wind effect even for large heating amplitudes (Fig. 6c).

In the REF experiment with a polar vortex, downwelling maximizes at the equatorward edge of the polar vortex in the lower stratosphere (not shown) which is consistent with a localized temperature increase in response to a strengthened residual circulation in the same region in the neutral polar vortex regime (Fig. 6b). The localized warming of the lower stratosphere in the REF experiment is associated with a slightly weaker attenuation of zonal-mean zonal winds above the tropospheric jet than in the NPV experiment. Additionally, zonal-mean zonal winds are strengthened on the poleward side of the localized heating, which represents the equatorward side of the lower polar vortex. This feature of a strengthened residual circulation in the neutral regime—namely, accelerating the equatorward edge of the lower polar vortex and thereby shifting the lower vortex equatorward—is the crucial point that is associated with the change in polar vortex geometry that eventually induces the transition to the strong regime.

The convergence of the poleward migrating tropospheric jet and the equatorward shifting lower-stratospheric polar vortex also explains the lower efficiency of the critical-layer control mechanism for synoptic-scale waves and, hence, contributes to the slower strengthening of the lower-stratospheric residual circulation in the REF experiment (Fig. 3c). Whenever the critical layer around 40°N rises, the region of wave dissipation between the tropospheric jet and the lower-stratospheric polar vortex shrinks. This will eventually terminate the critical-layer rise mechanism for synoptic-scale waves at $q_0 = 0.3$ K day^{-1} representing the first critical point (CP1) in the schematic of Fig. 1.

The results above confirm hypothesis 2. Due to the localized region of maximum downwelling at the equatorward edge of the polar vortex in the REF experiment, a strengthened shallow branch of the residual circulation is consistent with an equatorward shift of the lower-stratospheric polar vortex in the neutral polar vortex regime. In light of the NPV experiment, which shows that planetary-scale wave flux requires a sufficiently pole- and upward expansion of the tropospheric jet to reach subtropical latitudes, the equatorward shift of the lower-stratospheric polar vortex can also be
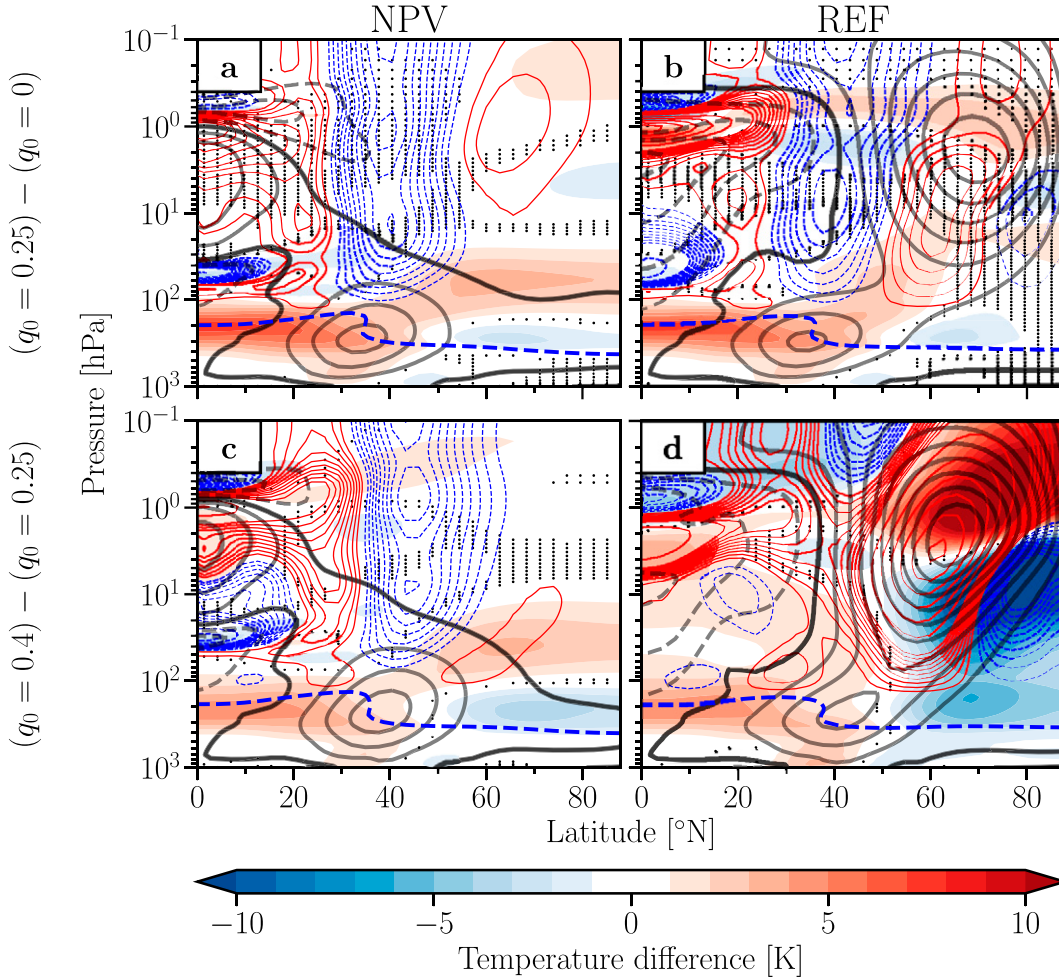
FIG. 6. Zonal-mean temperature differences $\Delta\overline{T}_{q_0}$ (color shading) (a),(b) between climate states at $q_0 = 0.25$ K day^{-1} and $q_0 = 0$ as well as (c),(d) between climate states at $q_0 = 0.4$ and $q_0 = 0.25$ K day^{-1} as functions of latitude and pressure for the (a),(c) NPV and (b),(d) REF experiments. Dotted regions show temperature differences that are not significant at a 95% confidence level. Furthermore, the positive (negative) thermal-wind effect $\Delta\overline{u}_{\text{th}}$ of temperature differences above 150 hPa is shown by thin red solid (thin blue dashed) contour lines starting at 1 m s^{-1} (-1 m s^{-1}) with a contour interval of 1 m s^{-1} below a magnitude of 10 m s^{-1} and with a contour interval of 5 m s^{-1} above a magnitude of 10 m s^{-1}. Details of the computation of $\Delta\overline{u}_{\text{th}}$ are provided in the body text around Eqs. (4)–(6). Zonal-mean zonal winds (gray contour lines with a contour interval of 10 m s^{-1}, negative contours dashed, black zero-contour line) and lapse-rate tropopauses (thick blue dashed lines; WMO 1957) at (a),(b) $q_0 = 0.25$ K day^{-1} and at (c),(d) $q_0 = 0.4$ K day^{-1} are added.

associated with the equatorward shift of wave drag in the lower stratosphere (Figs. 4e and 5e).

7. Hypothesis 3: Reorganization of EP fluxes

The first step toward the transition to the strong polar vortex regime in the REF experiment happens at the intermediate state $q_0 = 0.3$ K day^{-1} when the tropospheric jet and the lower-stratospheric polar vortex have reached a critical minimum distance, shrinking the region of possible synoptic-scale wave dissipation to the point that the critical-layer control mechanism terminates (CP1 in Fig. 1). The increase of upward synoptic-scale wave flux at 100 hPa stops (Fig. D1f)

accompanied by a weakening of the lower-stratospheric residual circulation (Fig. 3c), and the meridional EP flux component at 40°N changes from pole- to equatorward (Fig. D1i). This is consistent with a slightly enhanced poleward shift of the tropospheric jet compared to the NPV experiment (Fig. 3a). Simultaneously, the polar vortex strengthens (Fig. 3b) consistent with reduced high-latitude downwelling (not shown). The climate state at $q_0 = 0.35$ K day^{-1} exhibits only a small additional poleward shift of the tropospheric jet compared to the climate state before, hence also counting as an intermediate state between the neutral and the strong polar vortex regime. The contribution of synoptic-scale wave flux to the lower-stratospheric residual circulation strength further
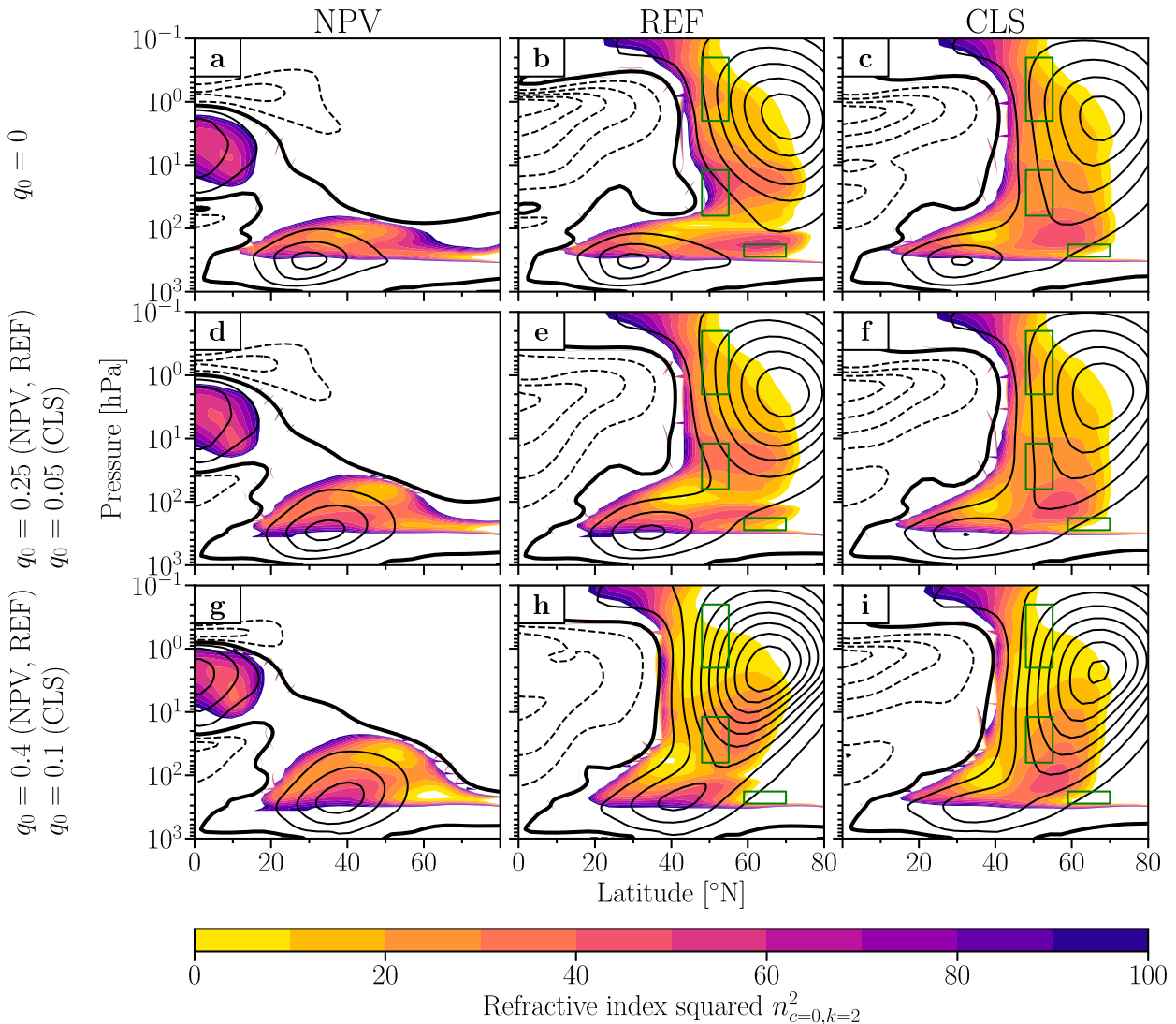
FIG. 7. Refractive index squared $n^2_{c=0,k=2}$ for stationary waves of wavenumber 2 (color shading with a contour interval of 10) and zonal-mean zonal winds (black contour lines with a contour interval of 10 m s^{-1}, negative contours dashed, thick zero-contour line) as functions of latitude and pressure for control-run climatologies of the (a) NPV, (b) REF, and (c) CLS experiments, as well as for heating amplitudes q_0 associated with climate states that are (d)–(f) at the end of the neutral and (g)–(i) already in the strong polar vortex regime. Note that different heating amplitudes are used for the REF and CLS experiments apart from the control runs as noted on the left-hand side of each row. In the case of the NPV experiment, the same heating amplitudes are chosen as for the REF experiment. The green boxes in the panels of the REF and CLS experiments indicate regions over which $n^2_{c=0,k=2}$ is averaged in Fig. 8.

decreases, which is consistent with further increases in the lower-stratospheric polar vortex strength. In contrast to this, planetary-scale contributions to the lower-stratospheric residual circulation strength still increase withholding the strong polar vortex regime (Fig. 3c).

The transition to the strong polar vortex regime in the REF experiment is completed at the second critical point at $q_0 = 0.4$ K day^{-1} (CP2 in Fig. 1) when the dissipation of planetary-scale EP flux is strongly reduced in the entire stratosphere (Fig. 5h). Large amounts of previously upward-propagating wave activity are instead refracted equatorward in the troposphere, which is consistent with the largest

poleward shift of the tropospheric jet compared to the NPV experiment. The residual circulation weakens significantly (Fig. 3c) with a large decrease of downwelling in the polar lower stratosphere (not shown). The previously negative feedback of the residual circulation on the polar vortex strength disappears, and a stronger negative meridional temperature gradient is consistent with a stronger polar vortex (Fig. 6d).

Analyzing the refractive index for stationary waves of wavenumber 2 displayed in Fig. 7, the evolution of planetary-scale wave fluxes can be explained. In the control run of the REF experiment, a thin layer of low refractive index below a

value of 10 is found below the polar vortex (Fig. 7b). The convergence of the poleward-moving tropospheric jet and the equatorward-moving lower stratospheric polar vortex due to TUTW improves the waveguide in the lower stratosphere (Fig. 7e), consistent with increasing upward wave flux in addition to the critical-layer rise in the subtropics (Fig. D1e). At $q_0 = 0.4$ K day^{-1}, the onset of the strong polar vortex regime, however, tropospheric and stratospheric wind structures have sufficiently merged to develop a latitudinally narrow waveguide confined by a thick layer of low refractive index at the top of the polar vortex. As revealed by Perlwitz and Harnik (2003) and Shaw et al. (2010), these two features of the waveguide are associated with downward wave coupling events, i.e., reflections of planetary-scale waves with significant impact on the troposphere.[7]

Indeed, the onset of the strong polar vortex regime is marked by a sharp decrease of upward planetary-scale wave flux in the stratosphere (Figs. 5h and D1e) which is associated with a sharp increase in the number of events of downward wavenumber-2 flux lasting up to 11 days (Fig. D2e), consistent with the increasing probability P of downward wavenumber-2 flux (Fig. 3d or D2b). In case of the NPV experiment, the frequency of downward wavenumber-2 flux events in the lower stratosphere also increases in response to TUTW (Fig. 3d or Fig. D2a), but upward planetary-scale wave flux always increases in response to TUTW (Fig. D1e) consistent with the steady upward expansion of the tropospheric jet. The emerging downward component of planetary-scale wave flux in the NPV experiment is negligible compared to the strong increase in upward wave flux events in response to TUTW (not shown). Furthermore, the duration of the majority of downward wavenumber-2 flux events stays below 4 days (Fig. D2d). In reanalysis data, reflection events of planetary-scale waves have been observed to couple the midstratosphere to the midtroposphere on time scales of about 1 week (Perlwitz and Harnik 2003, 2004). In this regard, we assume that proper wave-reflection events coupling the stratosphere to the troposphere only occur in the strong polar vortex regime of the REF experiment,[8] whereas the increase in downward wave flux events in the NPV experiment is attributed to enhanced variability of alternating up- and downward fluxes (not shown).

The results above confirm hypothesis 3. The circulation changes induced by TUTW—the poleward-moving tropospheric jet and the equatorward-moving lower-stratospheric polar vortex—support enhanced upward propagation of planetary-scale waves in the neutral polar vortex regime by generating a better waveguide in the midlatitude lower

stratosphere. When tropospheric and lower stratospheric jets have sufficiently converged, the waveguide for planetary-scale waves develops a reflective geometry. This represents the second critical point (CP2 in Fig. 1) where the transition to the strong polar vortex regime is completed.

8. Hypothesis 4: Enhanced poleward shift of the tropospheric jet

The probability for reflected waves to exert a considerable influence on the troposphere via downward wave coupling is assumed to be small in the neutral polar vortex regime consistent with the lack of a confined meridional waveguide owing to the weak meridional curvature of the zonal-mean flow (Figs. 7b,e). Instead, wave dissipation close to critical surfaces in the subtropics is much more relevant (Shaw et al. 2010) as shown in Figs. 5b and 5e. Only in the strong polar vortex regime, a considerable influence on the troposphere is observed according to the enhanced poleward shift of the tropospheric jet compared to the experiment without a polar vortex (Fig. 3a) which is consistent with the strong meridional curvature of the mean flow (Fig. 7h).

Perlwitz and Graf (2001) and Shaw and Perlwitz (2013) also found that wave activity which is reflected back into the troposphere propagates equatorward. Consistently, the sharp decrease of upward wave flux (Fig. D1e) associated with enhanced wave reflection during the regime transition toward $q_0 = 0.4$ K day^{-1} in our experiments with a polar vortex is accompanied by a sharp increase of equatorward wave flux compared to the NPV experiment (Fig. D1h) that is associated with the enhanced poleward shift of the tropospheric jet in the REF experiment compared to the NPV experiment. Thus, the transition of the waveguide from a nonreflective geometry in the neutral to a reflective geometry in the strong polar vortex regime appears to be crucial for the enhanced poleward shift of the tropospheric jet.

The results presented above confirm hypothesis 4. During the transition to the strong polar vortex regime beyond CP2, the tropospheric jet experiences an enhanced poleward shift compared to the tropospheric jet of the NPV experiment. Together with the confined meridional waveguide and the large number of downward wave-flux events, the significant impact on the troposphere provides strong evidence for downward wave coupling in the strong polar vortex regime.

9. Robustness of the dynamical mechanism

In this section, we test the robustness of the proposed dynamical mechanism responsible for the polar vortex regime transition. At first, we briefly recapitulate the proposed hypotheses for the CLS experiment. In the control run ($q_0 = 0$) of the CLS experiment, the polar vortex is already in a state close to the regime transition (Garny et al. 2020). The colder polar lower stratosphere compared to the REF experiment supports an already further equatorward located and stronger lower-stratospheric polar vortex providing a much better waveguide for planetary-scale waves in the lower stratosphere (Fig. 7c). Consistently, the planetary-scale EP flux across the

---

[7] We emphasize that the refractive index squared $n_{c,k}^2$ used in our study is only suitable to assess the general ability of wave propagation in the meridional plane. In order to classify the waveguide of the strong polar vortex regime as a waveguide that causes downward wave coupling events, the computation of separate refractive indices for meridional and vertical wave propagation is necessary as demonstrated by Harnik and Lindzen (2001).

[8] The sharp increase of downward wave-flux events in the CLS experiment is discussed in section 9.
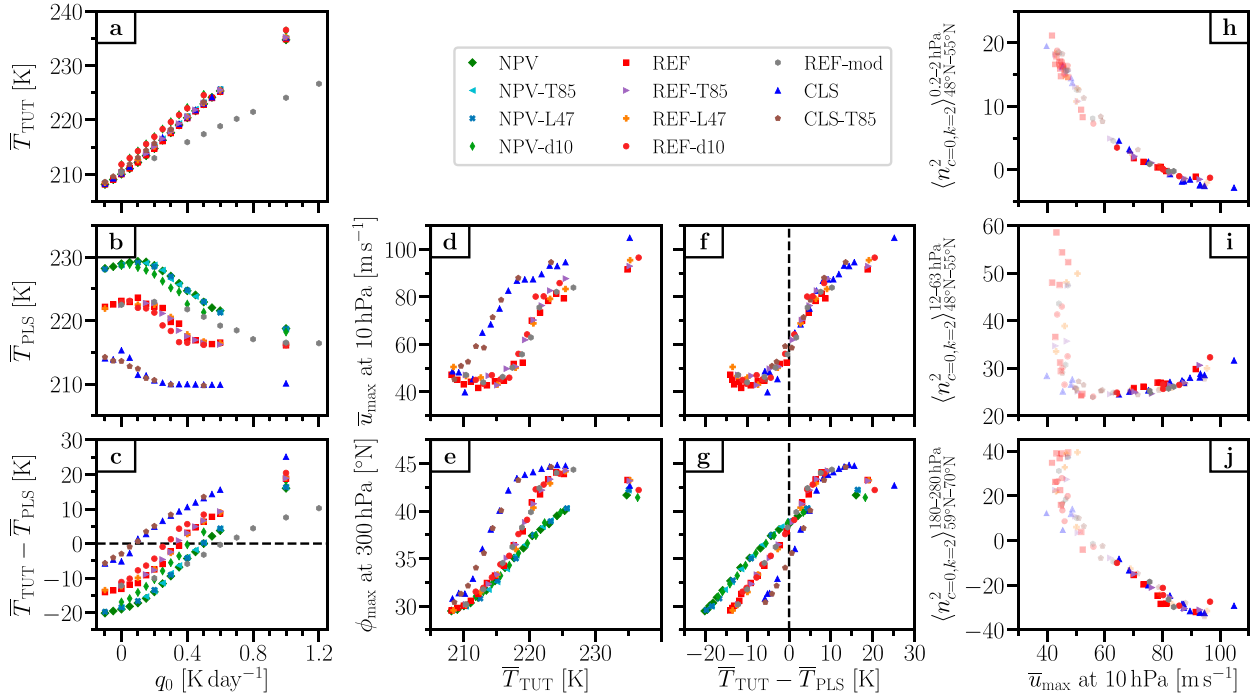
FIG. 8. (a) Average tropical upper-tropospheric temperature $\overline{T}_{\mathrm{TUT}} := \langle \overline{T} \rangle_{25°S–25°N}^{150–280\mathrm{hPa}}$, (b) average polar lower-stratospheric temperature $\overline{T}_{\mathrm{PLS}} := \langle \overline{T} \rangle_{65°N–90°N}^{180–280\mathrm{hPa}}$, and (c) their difference $\overline{T}_{\mathrm{TUT}} - \overline{T}_{\mathrm{PLS}}$ as functions of the heating amplitude q_0, as well as (d),(f) $\overline{u}_{\max}$ at 10 hPa and (e),(g) $\phi_{\max}$ at 300 hPa as functions of (d),(e) $\overline{T}_{\mathrm{TUT}}$ and (f),(g) $\overline{T}_{\mathrm{TUT}} - \overline{T}_{\mathrm{PLS}}$, respectively, for all available NPV, REF, and CLS experiments. Furthermore, averages of the refractive index squared $n_{c=0,k=2}^2$ for stationary waves of wavenumber 2 for three different regions, namely, (h) 0.2–2 hPa and 48°–55°N, (i) 12–63 hPa and 48°–55°N, and (j) 180–280 hPa and 59°–70°N are shown as functions of $\overline{u}_{\max}$ at 10 hPa for all available experiments with a polar vortex. Nontransparent markers in (h)–(j) indicate climate states associated with the strong polar vortex regime with frequent downward-pointing wavenumber-2 Eliassen–Palm fluxes in the midlatitude lower stratosphere, i.e., with $P(B_{\mathrm{top}}^{\mathrm{WN2}} > 0) > 0.25$. The remaining climate states with $\overline{u}_{\max} > 60$ m s^{-1} exhibiting transparent markers are assumed to represent the strong polar vortex regime as well, but wavenumber-decomposed data have not been produced (for REF-L47 and CLS-T85) to confirm this.

100 hPa level in midlatitudes is almost 50% larger than in the REF experiment (Fig. D1e) corresponding to the pronounced probability of a weak polar vortex in the CLS control run (Fig. 3b), the stronger residual circulation (Fig. 3c), and the high frequency of sudden stratospheric warmings (Fig. A1b). On the other hand, a large number of downward wavenumber-2 events lasting up to 8 days are observed (Fig. D2f) which is consistent with the second pronounced peak of the probability distribution function of $\overline{u}_{\max}$ at 10 hPa at 70 m s^{-1} representing a strong polar vortex after reflection events (Shaw and Perlwitz 2013). In the neutral polar vortex regime of the CLS experiment ($q_0 \leq 0$), the strengthened lower-stratospheric residual circulation is associated with the critical-layer control mechanism. A weakly positive heating amplitude of $q_0 = 0.1$ K day^{-1} is, however, sufficient to trigger circulation changes that shift the lower-stratospheric polar vortex equatorward in the position suitable to form the reflective waveguide (Fig. 7i) consistent with a sharp increase in the number and duration of downward wave flux events (Fig. D2f). Correspondingly, the polar vortex strength increases (Fig. 3b) which is accompanied by an enhanced poleward shift of the tropospheric jet compared to the NPV experiment (Fig. 3a)

representing the strong polar vortex regime of the CLS experiment ($q_0 \gtrsim 0.1$ K day^{-1}).

Additionally, TUTW experiments are repeated with different resolutions (labeled "-T85" and "-L47"), different tropical stratification in the troposphere (labeled "-d10") and a different heating shape (labeled "-mod"; refer to Table 1 and section 3 for details). To unify the circulation responses due to different realizations of TUTW, the average tropical upper-tropospheric temperature $\overline{T}_{\mathrm{TUT}} := \langle \overline{T} \rangle_{25°S–25°N}^{150–280\mathrm{hPa}}$ is used. Figure 8a confirms the mainly linear relation between $\overline{T}_{\mathrm{TUT}}$ and the heating amplitude q_0 (Wang et al. 2012). Three groups of data points exist: one group for the large number of experiments with $\delta_z = 4.3$ K employing the standard heating defined in Eq. (2), one group for the NPV-d10 and REF-d10 experiments with $\delta_z = 10$ K employing the standard heating, and one group for the REF-mod experiment with $\delta_z = 4.3$ K employing the modified heating defined in Eq. (3). Both groups employing the standard heating share the same gradient of $\overline{T}_{\mathrm{TUT}}$ with respect to q_0, but the experiments with $\delta_z = 10$ K are slightly offset to higher temperatures. The experiment with modified heating shows a less strong gradient of $\overline{T}_{\mathrm{TUT}}(q_0)$.

Expressing the polar vortex strength ($\overline{u}_{\max}$ at 10 hPa) and the latitude of the tropospheric jet ($\phi_{\max}$ at 300 hPa) as functions of $\overline{T}_{\mathrm{TUT}}$, all experiments are clustered according to their stratospheric setups, regardless of the precise realization of tropospheric warming that increases $\overline{T}_{\mathrm{TUT}}$ (Figs. 8d,e). The REF (CLS) experiments exhibit a sharp strengthening of the polar vortex at $\overline{T}_{\mathrm{TUT}} \gtrsim 217\,\mathrm{K}$ ($\overline{T}_{\mathrm{TUT}} \gtrsim 210\,\mathrm{K}$) which is accompanied by an enhanced poleward shift of the tropospheric jet compared to the tropospheric jet of the NPV experiments.

The offset in the critical value of $\overline{T}_{\mathrm{TUT}}$ between the REF and CLS experiments can be attributed to temperature differences in the polar lower stratosphere. This is due to the fact that REF and CLS experiments are forced with different stratospheric equilibrium temperatures being most pronounced in the polar lower stratosphere. Figure 8b shows a nonlinear relation of the average temperature $\overline{T}_{\mathrm{PLS}} := \langle \overline{T} \rangle_{65°-90°\mathrm{N}}^{180-280\mathrm{hPa}}$ in the polar lower stratosphere as a function of q_0 for all experiments consistent with their respective residual circulation strengths (cf. Fig. 7 of Wang et al. 2012). Remarkably, the different stratospheric conditions of REF and CLS experiments can be reconciled when the polar vortex strength is displayed as a function of $\overline{T}_{\mathrm{TUT}} - \overline{T}_{\mathrm{PLS}}$ (Fig. 8f). Furthermore, the sharp strengthening of the polar vortex during the transition from the neutral to the strong regime seems to occur near $\overline{T}_{\mathrm{TUT}} = \overline{T}_{\mathrm{PLS}}$. While $\overline{T}_{\mathrm{PLS}}$ is strongly coupled to the polar vortex strength, we emphasize that thermal forcings differ between the REF and CLS experiments in the polar lower stratosphere.

Testing the proposed mechanism of the previous section regarding the changes of the waveguide accompanying the regime transition, averages of the refractive index squared for stationary wavenumber-2 waves $n_{c=0,k=2}^2$ for three different regions are shown in Figs. 8h–j as functions of the polar vortex strength.[9] At a first glance, the conformity of the entire set of experiments with a polar vortex is visible and confirms that a unique behavior of the waveguide as a function of the polar vortex strength is observed in this study regardless of tropospheric or stratospheric realizations. The roughly linear decrease of the refractive index at the top of the polar vortex with increasing polar vortex strength suggests that the probability of the formation of a reflecting surface in the upper stratosphere rather gradually increases from the neutral to the strong regime (Fig. 8h; Harnik and Lindzen 2001). Thus, enhanced occurrence of reflecting surfaces in the upper stratosphere is not able to explain the sharp strengthening of the polar vortex during the regime transition. Instead, the transition to the strong polar vortex regime with $P > 0.25$ is only observed after a minimum of the refractive index on the equatorward side as well as a sufficiently wide region of negative refractive index on the poleward side of the polar vortex are simultaneously reached (Figs. 8i,j). Small values of the refractive index on the equatorward side of the polar vortex are indicative of a region of wave evanescence (Harnik and Lindzen 2001) which is necessary in combination with the region of wave evanescence on the poleward side of the polar

vortex to develop the confined geometry of the waveguide that prevents wave dissipation in the stratosphere and promotes downward wave coupling events (Perlwitz and Harnik 2003; Shaw et al. 2010). The slight increase in average refractive index values on the equatorward side of the polar vortex in the strong polar vortex regime is associated with the equatorward shift of the polar vortex, bringing higher values of the refractive index into the fixed region that is used for averaging (Fig. 8i).

Although the presumed regions of wave evanescence have to be confirmed (see footnote 7), the consistent formation of a confined waveguide with reflective geometry in all experiments when the polar vortex sharply strengthens together with the enhanced poleward shift of the tropospheric jet compared to the experiments without a polar vortex supports downward wave coupling as the relevant process for the regime transition.

10. Discussion

The results of sections 4–9 confirm the hypotheses proposed in section 2, which helped to establish the schematic of the dynamical mechanism for the transition to the strong polar vortex regime in Fig. 1. Some parts of the dynamical mechanism require, however, further investigations.

The equatorward shift of the lower polar vortex in the REF experiments proceeds nonlinearly (not shown) in contrast to the linear strengthening of the lower-stratospheric residual circulation in the neutral polar vortex regime. This hints at a critical poleward and upward expansion of the tropospheric jet in the REF experiments for which sufficient amount of planetary-scale wave flux is refracted equatorward to induce the equatorward shift of the lower polar vortex. This is supported by the NPV experiments, where in absence of a polar vortex a sufficient pole- and upward expansion of the tropospheric jet is necessary for planetary-scale waves to reach the subtropical lower stratosphere. The exact interplay between enhanced equatorward planetary-scale EP flux, the equatorward shift of the lower-stratospheric polar vortex and the thermal structure of the lower stratosphere can, however, not be disentangled by steady-state simulations.

Further, it remains to be clarified whether the somewhat unrealistic representation of the tropospheric dynamics with merging and separating of the subtropical and the eddy-driven jets in the dry dynamical-core model influences the response to TUTW in the lower stratosphere (Lu et al. 2010). To prove the relevance of the proposed dynamical mechanism, future studies should adjust the setup to reduce the unrealistically large autocorrelation time scales, e.g., by modifying tropospheric equilibrium temperatures via the asymmetry parameter (Chan and Plumb 2009; Sheshadri and Plumb 2017).

Another part of the mechanism that needs to be confirmed is the presence of downward wave coupling events in the strong polar vortex regime. The characteristics of a waveguide enabling downward wave coupling events (Perlwitz and Harnik 2003; Shaw et al. 2010) have to be detected with separate refractive indices for meridional and vertical propagation of planetary-scale waves (Harnik and Lindzen 2001). Nevertheless, we find similarities of the general refractive index squared $n_{c,k}^2$

---

[9] The three regions over which $n_{c=0,k=2}^2$ is averaged in Figs. 8h–j are visualized in Fig. 7 by green boxes.

for propagation in the meridional plane between the neutral and strong polar vortex regimes of our study and two episodes of the 1996 Southern Hemisphere winter characterized by separate refractive indices to represent one nonreflective and one reflective episode [cf. our Fig. 7 with Fig. 5 of Harnik and Lindzen (2001)]. In the neutral polar vortex regime as well as during the nonreflective episode, $n_{c,k}^2$ exhibits contour lines that are equatorward tilted with height in the high-latitude upper stratosphere as well as a meridionally broad positive region. In contrast to this, in the strong polar vortex regime as well as during the reflective episode, the zero-contour line of $n_{c,k}^2$ in the high-latitude upper stratosphere is horizontally aligned and the meridional extent of the waveguide in the middle stratosphere is more confined. In addition to separate refractive indices for meridional and vertical wave propagation, future work needs to confirm the downward planetary-scale wave coupling between the stratosphere and troposphere, e.g., by time lagged correlations (Perlwitz and Graf 2001; Perlwitz and Harnik 2003, 2004; Shaw et al. 2010; Shaw and Perlwitz 2013).

11. Summary and conclusions

We performed simulations with an idealized general circulation model to investigate the transition of the stratospheric polar vortex to a strong and stable regime in response to tropical upper-tropospheric warming (TUTW). To this end, we reproduced the experiment of Wang et al. (2012) in presence of a polar vortex providing us with a reference experiment. We confirmed that the polar vortex regime transition is accompanied by a reorganization of Eliassen–Palm (EP) fluxes with less wave activity entering the stratosphere and more wave activity being refracted equatorward in the troposphere. Extending the work by Wang et al. (2012), we were able to reveal the dynamical mechanism responsible for the regime transition (Fig. 1) and to quantify its corresponding influence on the troposphere by repeating the simulated tropical-warming levels of the reference experiment, but without a polar vortex.

The response of the stratospheric circulation to TUTW is dominated by the critical-layer control mechanism (Shepherd and McLandress 2011) for all heating amplitudes in a state without a polar vortex, and for heating amplitudes below a certain threshold in the state with a polar vortex. Rising critical layers for planetary-scale Rossby waves enable stronger EP flux to enter the lower stratosphere, which is consistent with a strengthened residual circulation. In presence of a polar vortex, the residual circulation exhibits a localized region of maximum downwelling at its equatorward edge. Strengthening the residual circulation via the critical-layer control mechanism influences the thermal structure of the lower stratosphere in a way that is consistent with an equatorward shift of the lower-stratospheric polar vortex. The transition to the strong polar vortex regime occurs when the poleward-moving tropospheric jet and the equatorward-moving lower-stratospheric polar vortex develop a confined waveguide that reflects planetary-scale waves back to the troposphere where they are refracted equatorward (Perlwitz and Graf 2001; Shaw and Perlwitz 2013). This is accompanied by an enhanced poleward shift of the tropospheric jet compared to the experiment without a polar

vortex. A large set of sensitivity experiments with modified thermal forcing provides strong evidence that the polar vortex regime transition is robustly linked to the development of a reflective waveguide. Consequently, the stratospheric modulation of the troposphere in presence of the strong polar vortex regime is supposed to be linked to an enhanced occurrence of downward wave coupling events of planetary-scale waves (Perlwitz and Harnik 2003; Shaw et al. 2010).

The revealed dynamical mechanism in this idealized model study might be relevant for explaining circulation changes detected in complex climate models. In particular, the strengthening of the Southern Hemisphere polar vortex (Jucker et al. 2021), and the variable and nonlinear response of the NH polar vortex to global warming (Manzini et al. 2014, 2018; Simpson et al. 2018; Kretschmer et al. 2020) are not fully understood. Some circulation changes that are crucial to our proposed mechanism are observed in complex climate models, e.g., the strengthening of the residual circulation associated with the upper-flank strengthening of the subtropical jets (Shepherd and McLandress 2011; Hardiman et al. 2014; Abalos et al. 2021), the equatorward shift of the lower-stratospheric polar vortex (Butchart et al. 2010; Scaife et al. 2012), and the poleward migration of the tropospheric jets (Kushner et al. 2001; Barnes and Polvani 2013). The dependence of the critical warming level on the stratospheric basic state as shown here might help to explain the large spread in future climate projections (Manzini et al. 2014; Simpson et al. 2018). A sensitivity experiment with colder polar lower stratosphere showed that temperature increases of the tropical upper troposphere beyond 2 K are sufficient to trigger the regime transition, whereas temperature increases beyond 8 K are necessary in the reference experiment. The sharp regime transition found in the idealized model might, however, be blurred in complex models due to a broader spectrum of planetary-scale waves, transient effects of the annual cycle, and Arctic amplification. The relevance of the introduced dynamical mechanism beyond idealized climate models remains to be investigated.

APPENDIX A

Sudden Stratospheric Warming Frequency

The sudden stratospheric warming frequencies for the REF and CLS experiments are shown in Fig. A1b in comparison with 1989–2019 December–February (DJF) ERA5
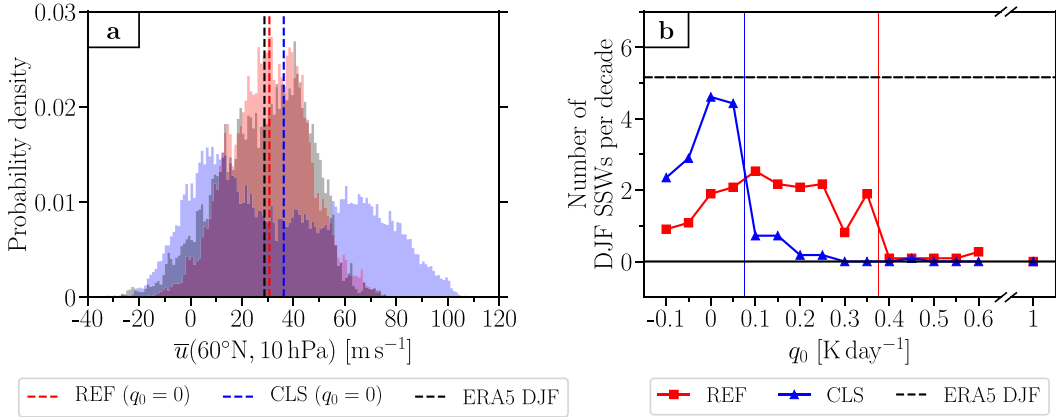
FIG. A1. (a) Probability densities (shading) and time-mean values (dashed vertical lines) of the zonal-mean zonal wind $\overline{u}$ at 60°N and 10 hPa for the REF and CLS control runs ($q_0 = 0$), as well as for ERA5 data for 1989–2019 during December–February (DJF) seasons and (b) the number of sudden stratospheric warmings (SSWs) per decade that form during DJF seasons for the REF and CLS experiments as a function of the tropical upper-tropospheric heating amplitude q_0, as well as for ERA5 data for 1989–2019 during DJF seasons (black dashed horizontal line). Red and blue vertical lines indicate the transitions to the strong polar vortex regime in the REF and CLS experiments, respectively.

data (Hersbach et al. 2020). The algorithm to detect sudden stratospheric warmings is based on Charlton and Polvani (2007). After the total number of sudden warmings n_{total} has been counted in each dataset, the sudden stratospheric warming frequency per decade is computed via $n_{total} \times 10/n_{DJF}$, where n_{DJF} is the number of DJF seasons covered by the dataset. In case of the 31-yr-spanning ERA5 dataset, $n_{total} = 16$, and $n_{DJF} = 31$. In case of the 9956-day-spanning REF and CLS experiments (spinup excluded), $n_{DJF} = 9956/90 \approx 111$.

APPENDIX B

Latitudes of Jet Maxima

The following algorithm is used for the calculation of the latitude ϕ_{max} of the maximum zonal-mean zonal wind $\overline{u}_{max}$ at a given pressure level:

1) Determine the absolute maximum zonal-mean zonal wind $\overline{u}_{max} \equiv \overline{u}_{i_{max}}$ in the Northern Hemisphere.
2) Collect the two adjacent data points northward and southward of $\overline{u}_{max}$, respectively, to obtain datasets $\overline{u}^{peak}$ and ϕ^{peak} for the zonal-mean zonal wind and the latitude around the peak, respectively:

$$\overline{u}^{peak} = [\overline{u}_{i_{max}-2}, \overline{u}_{i_{max}-1}, \overline{u}_{i_{max}}, \overline{u}_{i_{max}+1}, \overline{u}_{i_{max}+2}],$$

$$\phi^{peak} = [\phi_{i_{max}-2}, \phi_{i_{max}-1}, \phi_{i_{max}}, \phi_{i_{max}+1}, \phi_{i_{max}+2}] \cdot$$

3) Exclude elements $\overline{u}_i^{peak}$ and ϕ_i^{peak} from the datasets created in step 2 for which $0° \leq \phi_i^{peak} \leq 90°N$ is not fulfilled.
4) Transform $\overline{u}^{peak}$ to an array S ranging from 0 to 1 via (Adam et al. 2018)

$$\tilde{S} = \overline{u}^{peak} - \min(\overline{u}^{peak}),$$

$$S = \tilde{S}/\max(\tilde{S}) \cdot$$

5) Compute ϕ_{max} via Eq. (1) of Adam et al. (2018) using only data points of the peak:

$$\phi_{max} = \frac{\int_{\phi^{peak}} S(\phi)^n \phi \, d\phi}{\int_{\phi^{peak}} S(\phi)^n d\phi}, \tag{B1}$$

with $n = 6$. Note that in general $\phi_{max} \neq \phi_{i_{max}}$.

APPENDIX C

Strength of the Residual Circulation

In this study, strength and structure of the residual circulation (RC) are quantified via the downward-control streamfunction (Haynes et al. 1991)

$$\Psi_{dc}^* = \frac{2\pi a \cos(\phi)}{g} \int_0^p \frac{\overline{\mathcal{F}} + \overline{X}}{\hat{f}} dp' \tag{C1}$$

in the stationary limit of $\partial_t \overline{u} = 0$, where $\overline{\mathcal{F}} = [a\cos(\phi)]^{-1} \boldsymbol{\nabla} \cdot \mathbf{F}$ is the zonal-mean zonal wind tendency induced by the EP flux divergence $\boldsymbol{\nabla} \cdot \mathbf{F}$, $\overline{X}$ is parameterized drag, and $\hat{f} = [a\cos(\phi)]^{-1} \partial_\phi [\overline{u}\cos(\phi)] - f$ is proportional to the latitudinal derivative of angular momentum with Coriolis parameter $f = 2\Omega \sin(\phi)$ and Earth's rotation rate Ω, radius a, and gravitational acceleration g, respectively. The integral in Eq. (C1) is evaluated as in McLandress and Shepherd [2009; see their discussion of Eq. (3)]. The strength of the residual circulation at a given pressure level is then computed via $\max(\Psi_{dc}^*) - \min(\Psi_{dc}^*)$. Maximum and minimum of the streamfunction represent the turnaround latitudes of the circulation in the Northern and Southern Hemisphere, respectively, and are searched for at latitudes ϕ
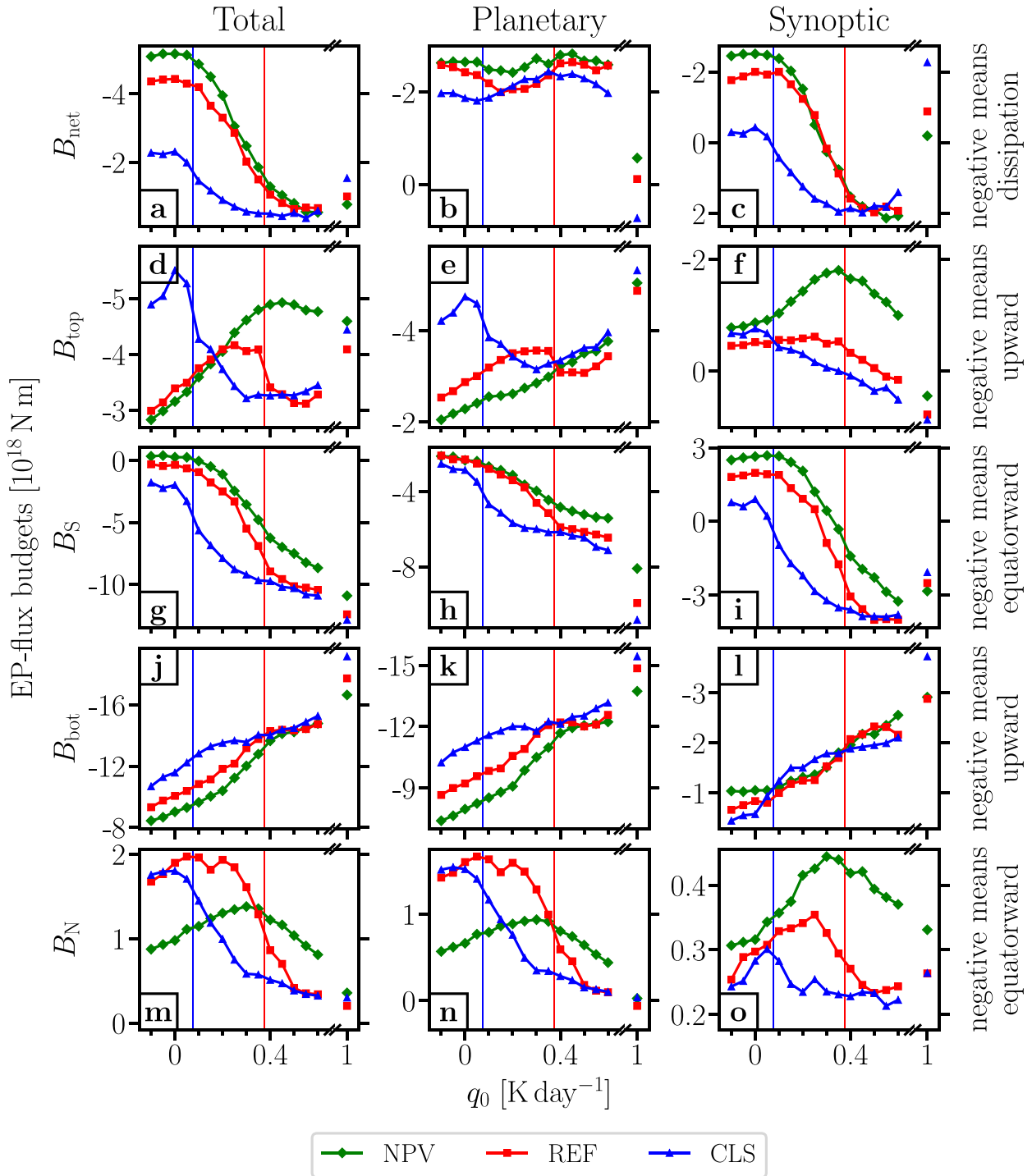
FIG. D1. (a)–(c) Total (all wavenumbers), planetary- (zonal wavenumbers 1–3), and synoptic-scale (zonal wavenumbers larger than 3) net EP flux budgets B_{net}, as well as the EP flux components (d)–(f) B_{top}, (g)–(i) B_S, (j)–(l) B_{bot}, and (m)–(o) B_N associated with the closed region defined by $\phi_S = 40°N$, $\phi_N = 60°N$, $p_{top} = 100$ hPa, and $p_{bot} = 300$ hPa as functions of the heating amplitude q_0 for the NPV, REF, and CLS experiments. Negative B_{top} and B_{bot} denote upward EP flux components, negative B_S and B_N denote equatorward EP flux components (in the Northern Hemisphere), and negative B_{net} denotes EP flux budget that dissipates within the region. Red and blue vertical lines indicate the transitions to the strong polar vortex regime in the REF and CLS experiments, respectively.
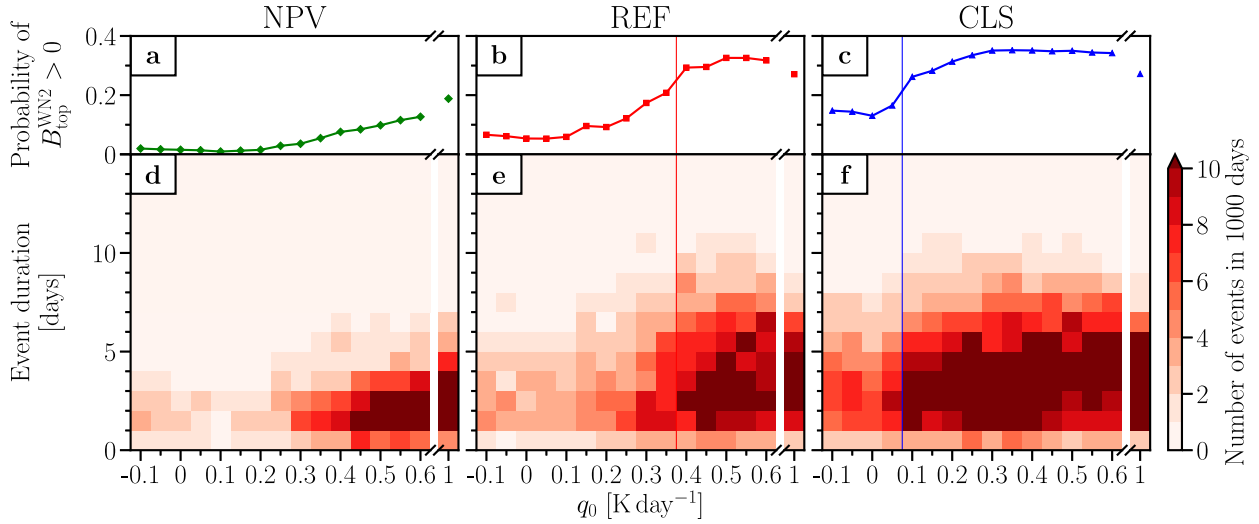
FIG. D2. (a)–(c) Probability that the wavenumber-2 vertical Eliassen–Palm flux B_{top}^{WN2} at 100 hPa integrated from 40° to 60°N is downward, as well as (d)–(f) the number of events of downward B_{top}^{WN2} as a function of the heating amplitude q_0 and the event duration for the (a),(d) NPV, (b),(e) REF, and (c),(f) CLS experiments. Note that with pressure as the vertical coordinate, downward wave flux is positive. Red and blue vertical lines indicate the transitions to the strong polar vortex regime in the REF and CLS experiments, respectively.

fulfilling $15° < |\phi| < 80°$, excluding the deep tropics and extreme polar regions which suffer from numerical inaccuracies. For the total residual circulation strength, $\overline{\mathcal{F}}$ is computed from all zonal wavenumbers, and $\overline{X}$ is computed from Rayleigh friction of the climatological-mean zonal-mean zonal wind in the sponge layer of EMIL. Contributions to the residual circulation strength from planetary- (zonal wavenumbers 1–3) and synoptic-scale (zonal wavenumbers larger than 3) wave drag are computed from Ψ_{dc}^* where only the planetary- and synoptic-scale $\overline{\mathcal{F}}$ is used, respectively, and $\overline{X}$ is set to zero.

APPENDIX D

Wave Fluxes Associated with a Closed Region

Wang et al. (2012) found a reorganization of EP fluxes with less wave activity propagating upward into the stratosphere and more wave activity propagating equatorward into the upper troposphere associated with the regime transition to a strong and stable polar vortex in response to tropical upper-tropospheric warming. To analyze the behavior of wave activity in the lower stratosphere in more detail, the isobaric EP-flux divergence (Andrews et al. 1983; Cohen et al. 2014)

$$\boldsymbol{\nabla} \cdot \mathbf{F} = \frac{\partial_\phi[F^{(\phi)}\cos(\phi)]}{a\cos(\phi)} + \partial_p F^{(p)} \quad (D1)$$

is integrated over the area given by $\phi_S \leq \phi \leq \phi_N$ and $p_{top} \leq p \leq p_{bot}$ which yields

$$\underbrace{\frac{2\pi a^2}{g}\int_{p_{top}}^{p_{bot}}\int_{\phi_S}^{\phi_N}\cos(\phi)\boldsymbol{\nabla}\cdot\mathbf{F}\,d\phi\,dp}_{B_{net}} = \underbrace{\frac{2\pi a\cos(\phi)}{g}\int_{p_{top}}^{p_{bot}}F^{(\phi)}\,dp\bigg|_{\phi_N}}_{B_N}$$

$$-\underbrace{\frac{2\pi a\cos(\phi)}{g}\int_{p_{top}}^{p_{bot}}F^{(\phi)}\,dp\bigg|_{\phi_S}}_{B_S}$$

$$+\underbrace{\frac{2\pi a^2}{g}\int_{\phi_S}^{\phi_N}\cos(\phi)F^{(p)}\,d\phi\bigg|_{p_{bot}}}_{B_{bot}},$$

$$-\underbrace{\frac{2\pi a^2}{g}\int_{\phi_S}^{\phi_N}\cos(\phi)F^{(p)}\,d\phi\bigg|_{p_{top}}}_{B_{top}}$$

(D2)

where $F^{(\phi)}$ and $F^{(p)}$ are latitudinal and vertical components of the EP flux vector $\mathbf{F}$, respectively.

To capture the wave activity changes associated with the regime transition best, we choose $\phi_S = 40°$N, $\phi_N = 60°$N, $p_{top} = 100$ hPa, and $p_{bot} = 300$ hPa as used in Fig. D1.[10] Confirming Wang et al. (2012), the main result is the reduced upward wave activity at 100 hPa (reduced negative B_{top}, Fig. D1d) and increased equatorward wave activity at 40°N (increased negative B_S, Fig. D1g) at the transitions to the strong polar vortex regime in the REF and CLS experiments. This result is robust when changing one of the

_____

[10] Note that ϕ needs to be given in radians when evaluating Eq. (D2).

region's boundaries while keeping the other ones fixed, at least for $30° \leq \phi_S \leq 40°N$, $60° \leq \phi_N \leq 90°N$, $30 \leq p_{top} \leq 100$ hPa, and $300 \leq p_{bot} \leq 590$ hPa (not shown). The reorganization of wave fluxes accompanying the transition to the strong polar vortex regime can be associated with more frequent and longer lasting events of downward wavenumber-2 EP fluxes as shown in Fig. D2, which is also robust for different extratropical latitude bands (not shown).

REFERENCES

Abalos, M., and Coauthors, 2021: The Brewer–Dobson circulation in CMIP6. *Atmos. Chem. Phys.*, **21**, 13 571–13 591, https://doi.org/10.5194/acp-21-13571-2021.

Adam, O., and Coauthors, 2018: The TropD software package (v1): Standardized methods for calculating tropical-width diagnostics. *Geosci. Model Dev.*, **11**, 4339–4357, https://doi.org/10.5194/gmd-11-4339-2018.

Andrews, D. G., J. D. Mahlman, and R. W. Sinclair, 1983: Eliassen-Palm diagnostics of wave–mean flow interaction in the GFDL "SKYHI" general circulation model. *J. Atmos. Sci.*, **40**, 2768–2784, https://doi.org/10.1175/1520-0469(1983)040<2768:ETWATM>2.0.CO;2.

Ayarzagüena, B., and Coauthors, 2020: Uncertainty in the response of sudden stratospheric warmings and stratosphere-troposphere coupling to quadrupled CO_2 concentrations in CMIP6 models. *J. Geophys. Res. Atmos.*, **125**, e2019JD032345, https://doi.org/10.1029/2019JD032345.

Baldwin, M. P., and T. J. Dunkerton, 2001: Stratospheric harbingers of anomalous weather regimes. *Science*, **294**, 581–584, https://doi.org/10.1126/science.1063315.

Barnes, E. A., and L. Polvani, 2013: Response of the midlatitude jets, and of their variability, to increased greenhouse gases in the CMIP5 models. *J. Climate*, **26**, 7117–7135, https://doi.org/10.1175/JCLI-D-12-00536.1.

Birner, T., and J. R. Albers, 2017: Sudden stratospheric warmings and anomalous upward wave activity flux. *SOLA*, **13A**, 8–12, https://doi.org/10.2151/sola.13A-002.

Butchart, N., and Coauthors, 2010: Chemistry–climate model simulations of twenty-first century stratospheric climate and circulation changes. *J. Climate*, **23**, 5349–5374, https://doi.org/10.1175/2010JCLI3404.1.

Butler, A. H., D. W. J. Thompson, and R. Heikes, 2010: The steady-state atmospheric circulation response to climate change–like thermal forcings in a simple general circulation model. *J. Climate*, **23**, 3474–3496, https://doi.org/10.1175/2010JCLI3228.1.

Chan, C. J., and R. A. Plumb, 2009: The response to stratospheric forcing and its dependence on the state of the troposphere. *J. Atmos. Sci.*, **66**, 2107–2115, https://doi.org/10.1175/2009JAS2937.1.

Charlton, A. J., and L. M. Polvani, 2007: A new look at stratospheric sudden warmings. Part I: Climatology and modeling benchmarks. *J. Climate*, **20**, 449–469, https://doi.org/10.1175/JCLI3996.1.

Cohen, N. Y., E. P. Gerber, and O. Bühler, 2014: What drives the Brewer–Dobson circulation? *J. Atmos. Sci.*, **71**, 3837–3855, https://doi.org/10.1175/JAS-D-14-0021.1.

Edmon, H. J., B. J. Hoskins, and M. E. McIntyre, 1980: Eliassen-Palm cross sections for the troposphere. *J. Atmos. Sci.*, **37**, 2600–2616, https://doi.org/10.1175/1520-0469(1980)037<2600:EPCSFT>2.0.CO;2.

Garny, H., R. Walz, M. Nützel, and T. Birner, 2020: Extending the Modular Earth Submodel System (MESSy v2.54) model hierarchy: The ECHAM/MESSy Idealized (EMIL) model setup. *Geosci. Model Dev.*, **13**, 5229–5257, https://doi.org/10.5194/gmd-13-5229-2020.

Gerber, E. P., 2012: Stratospheric versus tropospheric control of the strength and structure of the Brewer–Dobson circulation. *J. Atmos. Sci.*, **69**, 2857–2877, https://doi.org/10.1175/JAS-D-11-0341.1.

——, and L. M. Polvani, 2009: Stratosphere–troposphere coupling in a relatively simple AGCM: The importance of stratospheric variability. *J. Climate*, **22**, 1920–1933, https://doi.org/10.1175/2008JCLI2548.1.

Hardiman, S. C., N. Butchart, and N. Calvo, 2014: The morphology of the Brewer–Dobson circulation and its response to climate change in CMIP5 simulations. *Quart. J. Roy. Meteor. Soc.*, **140**, 1958–1965, https://doi.org/10.1002/qj.2258.

Harnik, N., and R. S. Lindzen, 2001: The effect of reflecting surfaces on the vertical structure and variability of stratospheric planetary waves. *J. Atmos. Sci.*, **58**, 2872–2894, https://doi.org/10.1175/1520-0469(2001)058<2872:TEORSO>2.0.CO;2.

Haynes, P. H., M. E. McIntyre, T. G. Shepherd, C. J. Marks, and K. P. Shine, 1991: On the "downward control" of extratropical diabatic circulations by eddy-induced mean zonal forces. *J. Atmos. Sci.*, **48**, 651–678, https://doi.org/10.1175/1520-0469(1991)048<0651:OTCOED>2.0.CO;2.

Held, I. M., 2005: The gap between simulation and understanding in climate modeling. *Bull. Amer. Meteor. Soc.*, **86**, 1609–1614, https://doi.org/10.1175/BAMS-86-11-1609.

——, and M. J. Suarez, 1994: A proposal for the intercomparison of the dynamical cores of atmospheric general circulation models. *Bull. Amer. Meteor. Soc.*, **75**, 1825–1830, https://doi.org/10.1175/1520-0477(1994)075<1825:APFTIO>2.0.CO;2.

Hersbach, H., and Coauthors, 2020: The ERA5 global reanalysis. *Quart. J. Roy. Meteor. Soc.*, **146**, 1999–2049, https://doi.org/10.1002/qj.3803.

Jucker, M., T. Reichler, and D. W. Waugh, 2021: How frequent are Antarctic sudden stratospheric warmings in present and future climate? *Geophys. Res. Lett.*, **48**, e2021GL093215, https://doi.org/10.1029/2021GL093215.

Karpechko, A. Y., and E. Manzini, 2017: Arctic stratosphere dynamical response to global warming. *J. Climate*, **30**, 7071–7086, https://doi.org/10.1175/JCLI-D-16-0781.1.

Kidston, J., A. A. Scaife, S. C. Hardiman, D. M. Mitchell, N. Butchart, M. P. Baldwin, and L. J. Gray, 2015: Stratospheric influence on tropospheric jet streams, storm tracks and surface weather. *Nat. Geosci.*, **8**, 433–440, https://doi.org/10.1038/ngeo2424.

Kim, B.-M., S.-W. Son, S.-K. Min, J.-H. Jeong, S.-J. Kim, X. Zhang, T. Shim, and J.-H. Yoon, 2014: Weakening of the stratospheric polar vortex by Arctic sea-ice loss. *Nat. Commun.*, **5**, 4646, https://doi.org/10.1038/ncomms5646.

Kim, J., and K.-Y. Kim, 2020: Characteristics of stratospheric polar vortex fluctuations associated with sea ice variability in the Arctic winter. *Climate Dyn.*, **54**, 3599–3611, https://doi.org/10.1007/s00382-020-05191-9.

Kretschmer, M., G. Zappa, and T. G. Shepherd, 2020: The role of Barents–Kara sea ice loss in projected polar vortex changes. *Wea. Climate Dyn.*, **1**, 715–730, https://doi.org/10.5194/wcd-1-715-2020.

Kushner, P. J., I. M. Held, and T. L. Delworth, 2001: Southern Hemisphere atmospheric circulation response to global

warming. *J. Climate*, **14**, 2238–2249, https://doi.org/10.1175/1520-0442(2001)014<0001:SHACRT>2.0.CO;2.

Lindgren, E. A., A. Sheshadri, and R. A. Plumb, 2018: Sudden stratospheric warming formation in an idealized general circulation model using three types of tropospheric forcing. *J. Geophys. Res. Atmos.*, **123**, 10 125–10 139, https://doi.org/10.1029/2018JD028537.

Lu, J., G. Chen, and D. M. W. Frierson, 2010: The position of the midlatitude storm track and eddy-driven westerlies in aquaplanet AGCMs. *J. Atmos. Sci.*, **67**, 3984–4000, https://doi.org/10.1175/2010JAS3477.1.

Maher, P., and Coauthors, 2019: Model hierarchies for understanding atmospheric circulation. *Rev. Geophys.*, **57**, 250–280, https://doi.org/10.1029/2018RG000607.

Manzini, E., and Coauthors, 2014: Northern winter climate change: Assessment of uncertainty in CMIP5 projections related to stratosphere-troposphere coupling. *J. Geophys. Res. Atmos.*, **119**, 7979–7998, https://doi.org/10.1002/2013JD021403.

——, A. Y. Karpechko, and L. Kornblueh, 2018: Nonlinear response of the stratosphere and the North Atlantic-European climate to global warming. *Geophys. Res. Lett.*, **45**, 4255–4263, https://doi.org/10.1029/2018GL077826.

Martineau, P., G. Chen, S.-W. Son, and J. Kim, 2018: Lower-stratospheric control of the frequency of sudden stratospheric warming events. *J. Geophys. Res. Atmos.*, **123**, 3051–3070, https://doi.org/10.1002/2017JD027648.

Matsuno, T., 1970: Vertical propagation of stationary planetary waves in the winter Northern Hemisphere. *J. Atmos. Sci.*, **27**, 871–883, https://doi.org/10.1175/1520-0469(1970)027<0871:VPOSPW>2.0.CO;2.

McLandress, C., and T. G. Shepherd, 2009: Simulated anthropogenic changes in the Brewer–Dobson circulation, including its extension to high latitudes. *J. Climate*, **22**, 1516–1540, https://doi.org/10.1175/2008JCLI2679.1.

Perlwitz, J., and H.-F. Graf, 2001: Troposphere-stratosphere dynamic coupling under strong and weak polar vortex conditions. *Geophys. Res. Lett.*, **28**, 271–274, https://doi.org/10.1029/2000GL012405.

——, and N. Harnik, 2003: Observational evidence of a stratospheric influence on the troposphere by planetary wave reflection. *J. Climate*, **16**, 3011–3026, https://doi.org/10.1175/1520-0442(2003)016<3011:OEOASI>2.0.CO;2.

——, and ——, 2004: Downward coupling between the stratosphere and troposphere: The relative roles of wave and zonal mean processes. *J. Climate*, **17**, 4902–4909, https://doi.org/10.1175/JCLI-3247.1.

Polvani, L. M., and P. J. Kushner, 2002: Tropospheric response to stratospheric perturbations in a relatively simple general circulation model. *Geophys. Res. Lett.*, **29**, 1114, https://doi.org/10.1029/2001GL014284.

Randel, W. J., and I. M. Held, 1991: Phase speed spectra of transient eddy fluxes and critical layer absorption. *J. Atmos. Sci.*,

48, 688–697, https://doi.org/10.1175/1520-0469(1991)048<0688:PSSOTE>2.0.CO;2.

Scaife, A. A., and Coauthors, 2012: Climate change projections and stratosphere–troposphere interaction. *Climate Dyn.*, **38**, 2089–2097, https://doi.org/10.1007/s00382-011-1080-7.

Shaw, T. A., 2019: Mechanisms of future predicted changes in the zonal mean mid-latitude circulation. *Curr. Climate Change Rep.*, **5**, 345–357, https://doi.org/10.1007/s40641-019-00145-8.

——, and J. Perlwitz, 2013: The life cycle of Northern Hemisphere downward wave coupling between the stratosphere and troposphere. *J. Climate*, **26**, 1745–1763, https://doi.org/10.1175/JCLI-D-12-00251.1.

——, ——, and N. Harnik, 2010: Downward wave coupling between the stratosphere and troposphere: The importance of meridional wave guiding and comparison with zonal-mean coupling. *J. Climate*, **23**, 6365–6381, https://doi.org/10.1175/2010JCLI3804.1.

Shepherd, T. G., and C. McLandress, 2011: A robust mechanism for strengthening of the Brewer–Dobson circulation in response to climate change: Critical-layer control of subtropical wave breaking. *J. Atmos. Sci.*, **68**, 784–797, https://doi.org/10.1175/2010JAS3608.1.

Sheshadri, A., and R. A. Plumb, 2017: Propagating annular modes: Empirical orthogonal functions, principal oscillation patterns, and time scales. *J. Atmos. Sci.*, **74**, 1345–1361, https://doi.org/10.1175/JAS-D-16-0291.1.

——, ——, and E. P. Gerber, 2015: Seasonal variability of the polar stratospheric vortex in an idealized AGCM with varying tropospheric wave forcing. *J. Atmos. Sci.*, **72**, 2248–2266, https://doi.org/10.1175/JAS-D-14-0191.1.

Simpson, I. R., P. Hitchcock, R. Seager, Y. Wu, and P. Callaghan, 2018: The downward influence of uncertainty in the Northern Hemisphere stratospheric polar vortex response to climate change. *J. Climate*, **31**, 6371–6391, https://doi.org/10.1175/JCLI-D-18-0041.1.

Taylor, K. E., R. J. Stouffer, and G. A. Meehl, 2012: An overview of CMIP5 and the experiment design. *Bull. Amer. Meteor. Soc.*, **93**, 485–498, https://doi.org/10.1175/BAMS-D-11-00094.1.

Vallis, G. K., P. Zurita-Gotor, C. Cairns, and J. Kidston, 2015: Response of the large-scale structure of the atmosphere to global warming. *Quart. J. Roy. Meteor. Soc.*, **141**, 1479–1501, https://doi.org/10.1002/qj.2456.

Wang, S., E. P. Gerber, and L. M. Polvani, 2012: Abrupt circulation responses to tropical upper-tropospheric warming in a relatively simple stratosphere-resolving AGCM. *J. Climate*, **25**, 4097–4115, https://doi.org/10.1175/JCLI-D-11-00166.1.

WMO, 1957: Definition of the tropopause. *WMO Bull.*, **6**, 136–140.

Wu, Y., I. R. Simpson, and R. Seager, 2019: Intermodel spread in the Northern Hemisphere stratospheric polar vortex response to climate change. *Geophys. Res. Lett.*, **46**, 13 290–13 298, https://doi.org/10.1029/2019GL085545.